International Journal of Quantum Information
Vol. 4, No. 2 (2006) 233–296

World Scientific
www.worldscientific.com

QUANTUM DOT COMPUTING GATES

GOONG CHEN[*,‡], ZIJIAN DIAO[†], JONG U. KIM[§], ARUP NEOGI[‖], KERIM URTEKIN[‡,¶] and ZHIGANG ZHANG[*]

[*]*Department of Mathematics, Texas A&M University, College Station, TX 77843, USA*

[†]*Department of Mathematics, Ohio University-Eastern, St. Clairsville, OH 43950, USA*

[‡]*Institute for Quantum Studies, Texas A&M University, College Station, TX 77843, USA*

[§]*Department of Electrical Engineering, Texas A&M University, College Station, TX 77843, USA*

[‖]*Department of Physics, University of North Texas, Denton, TX 76203*

[¶]*Department of Physics, Texas A&M University College Station, TX 77843, USA*

Received 7 June 2005
Revised 10 November 2005

Semiconductor quantum dots are a promising candidate for future quantum computer devices. Presently, there are three major proposals for designing quantum computing gates based on quantum dot technology: (i) electrons trapped in microcavity; (ii) spintronics; (iii) biexcitons. We survey these designs and show mathematically how, in principle, they will generate 1-bit rotation gates as well as 2-bit entanglement and, thus, provide a class of universal quantum gates. Some physical attributes and issues related to their limitations, decoherence and measurement are also discussed.

Keywords: Quantum dots; quantum computing; universal quantum gates; spintronics; biexcitons; measurements.

1. Introduction

The design and construction of the quantum computer (QC) is a major scientific undertaking of the 21st Century. According to DiVincenzo,[13] five requirements must be satisfied in order to obtain a reliable QC system: (i) be scalable, (ii) the ability to initialize qubits, (iii) relatively long decoherence times (longer than the gate operation times), (iv) a qubit-specific read-out capability, and (v) a universal set of quantum gates.

Building devices to store and process computational bits quantum-mechanically (qubits) is a challenging problem. In a typical field-effect transistor (FET) in an electronic computer chip, 10,000 to 100,000 electrons participate in a single switching

event. It is impossible to isolate, out of such a complex system, two quantum mechanical states that would evolve coherently to play the role of a qubit.

Quantum dot (QD) fabrication is a major segment of contemporary nanotechnology. QD devices, including diode lasers, semiconductor optical amplifiers, IR (infrared) detectors, mid-IR lasers, quantum-optical single-photon emitters, etc. are being developed and considered for a wide variety of applications. QDs are also a promising candidate for future QC technology. In this paper, we hope to elucidate the connection between the physics of QDs and the basic mathematics of quantum gate operations. We have put a certain emphasis on the mathematical derivations but we also hope to explain some aspects of the rudimentary science and technology of QDs to the novice. This area of research is undergoing rapid advances and our paper is intended to be only a tutorial account rather than an exhaustive review. This paper targets a blend of researchers in physics, mathematics and engineering who work on the interdisciplinary study of quantum devices.

1.1. *QD properties and fabrication: From quantum wells, wires to quantum dots*

We begin by introducing what QDs are. QDs consist of nano-scale crystals from a special class of semiconductor materials, which are crystals composed of chemical elements in the periodic groups II-VI, III-V, or IV-IV. The size of QDs ranges from several to tens of nanometers (10^{-9} m) in diameter, which is about 10–100 atoms. A QD can contain from a single electron to several thousand electrons since the size of the quantum dot is designable. QDs are fabricated in semiconductor material in such a way that the free motion of the electrons is trapped in a quasi-zero-dimensional "dot." Because of the strong confinement imposed in all three spatial dimensions, QDs behave similarly to atoms and are often referred to as artificial atoms or giant atoms.

When a free electron is confined by a potential barrier, its continuous spectrum becomes discretized. In particular, the gap between two neighboring energy levels increases as the length where the free electron moves decreases. A similar thing happens in solid state. If the motion of electrons in the conduction band or that of the hole in the valence band is limited in a small region with a scale such as the De Broglie wavelength or a phase-coherence length,[a] then the conduction band or the valence band is split into subbands or discrete levels depending on the dimensionality of the confined structure: such is the case when a material with a lower bandgap is confined within a material with a higher bandgap. More efficient recombination of electron-hole pairs can be achieved by incorporation of a thin layer of a semiconductor material, with a smaller energy gap than the cladding layers, to form a double heterostructure. As the active layer thickness in a double heterostructure becomes

[a]If an electron travels far enough to be scattered by impurities or other electrons, it will lose its phase coherence (cf. the footnote on quantum coherence in Sec. 1.2). This is called *dephasing*. The length in which an electron travels yet can keep its phase coherent is called the phase coherence length.

close to the De Broglie wavelength (about 10 nm for semiconductor laser devices) or the Bohr exciton radius for lower dimensional structures, and as the motion of the electron is restricted within such a very small regime, energy quantization or momentum quantization is observed and quantum effects become apparent. Therefore, the electron states are not continuous but discrete. This phenomenon is known as the *size quantization effect*. A proposal for QD-based QC utilizes various energy levels of one or several electrons in QDs by confining those QDs in a *microcavity* will be studied in Sec. 2.

In natural bulk semiconductor material, the overwhelming majority of electrons occupy the valence band. However, an extremely small percentage of electrons may occupy the conduction band, which has higher energy levels. The only way for an electron in the valence band to be excited and be able to jump to the conduction band is to acquire enough energy to cross the *bandgap*. If such a jump or transition occurs, a new electric carrier in the valence band, called a *hole*, is generated. Since the hole moves in an opposite direction to the electron, the charge of a hole is regarded as positive. The pair of energy-raised electron and hole is called an *exciton*. The average physical separation between the electron and the hole is called the *exciton Bohr radius*. Excitons move freely in the bulk semiconductor. However, an exciton is trapped by high energy barriers as an electron is. The size quantization effect is optically observable. A proposal utilizing exciton (and also biexciton) energy levels for QC will be the topic of discussion in Sec. 4.

If the device length is smaller than the phase coherence length of the electron or exciton Bohr radius, the energy levels are discrete and the size quantization effect is observed. Since the energy levels are discrete, the three-dimensional energy band becomes lower-dimensional depending on the number of confinement directions. If there is only one directional length of device shorter than the phase coherence length, the device is regarded as a two-dimensional device, called a *quantum well*. The phase coherence length of a quantum well is about 1.62 μm for GaAs and about 0.54 μm for Si at low temperature. However, since the phase coherence length depends on impurity concentration, temperature, and so on, it can be modified for electronic applications. The exciton Bohr radius of GaAs is about 13 nm.

There are two approaches to fabricate nano-scale QDs: *top-down* and *bottom-up*. Semiconductor processing technologies, such as metal organic chemical vapor deposition, molecular beam epitaxy and e-beam lithography, etc. are used in the top-down approach. Surface and colloid chemistry such as self-assembly, vapor-liquid-solid techniques are used in the bottom-up approach.

There are many methods of synthesizing QDs in the bottom-up approach, such as chemical reactions in colloidal solutions, long time annealing in solid state, chemical vapor deposition on a solid surface, and wet or dry etching of thin film on a solid surface. Figure 1 shows a high resolution electron transmission microscopy (HRTEM) image of Cadmium Sulfide (CdS) nano-particles synthesized in a colloidal solution. It is shown that the triangular shaped CdS QD is crystalline. Even though crystalline QDs are synthesized relatively economically and conveniently in the bottom-up approach as compared with the top-down approach, the alignment

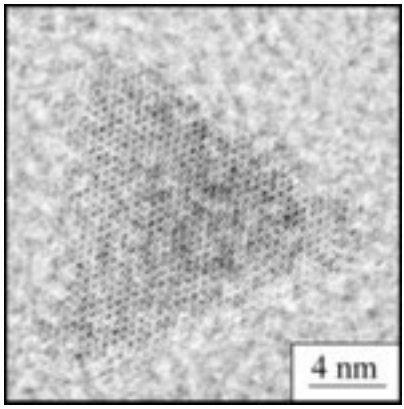

Fig. 1. HRTEM image of a triangular shaped Cadmium Sulfide (CdS) quantum dot. The quantum dot is crystalline (www.pinna.cx/albums/HRTEM/CdS_triangle.sized.jpg).

of QDs is a very serious problem for applications to QC even though such crystalline QDs have been made into a few optical devices, such as optical sensors or field effect diodes, and biomedical apparatus.

As mentioned above, several semiconductor processing technologies can be applied to QD fabrication in the top-down approach. Usually, a quantum well is the starting point of QD fabrication. Thus, let us first describe the technology of quantum well fabrication.

By molecular beam epitaxy and metal organic chemical vapor deposition techniques, an ultra-thin single crystalline layer can be deposited on a bulk substrate. The development of these advanced epitaxy techniques makes it possible to fabricate quantum wells with a very fine boundary. There are two types of quantum wells. One is formed by depositing several single crystalline layers through molecular beam epitaxy, or through the metal organic chemical vapor deposition technique. The other is by depositing single crystalline layers with modulated impurity concentration. The former is usually chosen for optoelectronic devices such as lasers where electrons and holes need to be confined at the same time, and the latter is for electronic devices where only either the electron or the hole needs to be confined.

A typical application of quantum wells with single crystalline layers is the AlGaAs/GaAs quantum well laser as shown in Fig. 2. An Aluminum Gallium Arsenide (AlGaAs) layer is deposited on a GaAs substrate and then a GaAs layer of thickness less than 100 nm is deposited on the AlGaAs layer, and AlGaAs layer is again deposited on the GaAs layer. The energy band profile shown in Fig. 2 is rotated by 90°. The thickness of the GaAs quantum well is about or less than the exciton Bohr radius and size quantization can be observed clearly. The electron and hole in the GaAs quantum well are confined by the AlGaAs energy barrier, respectively. The laser wavelength is dependent on the thickness of GaAs quantum well in the AlGaAs/GaAs quantum well laser.

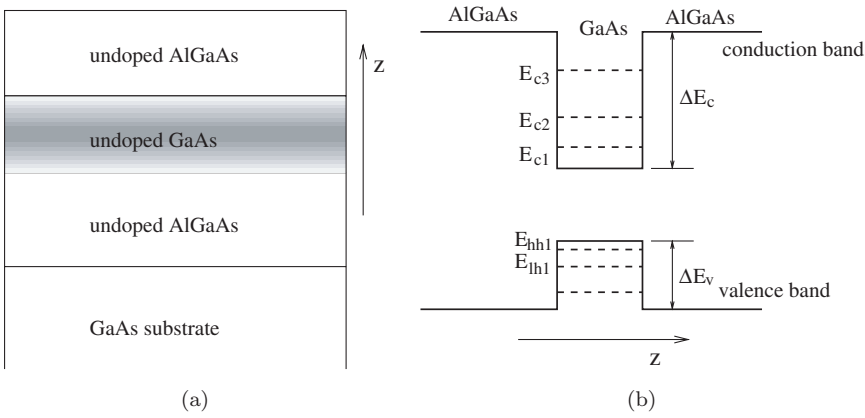

Fig. 2. An AlGaAs/GaAs quantum well structure: (a) cross-section and (b) conduction and valence band profile. The energy barrier heights of the conduction band and of the valence band are ΔE_c and ΔE_v, respectively. E_{ci} is the lowest energy of the ith conduction subband for $i = 1, 2$ and 3, E_{hh1} is the highest energy of the first heavy hole subband, and E_{lh1} is the highest energy of the light hole subband.

Remark 1. We briefly mention here some properties of semiconductor materials that are used in the fabrication of QDs.

Silicon oxide (SiO_2) has a low dielectric constant and is easily created by the oxidation of silicon; most electronic processors are made of silicon and silicon oxide. Such technology was developed by the silicon industry in the early 1960s. Nowadays, silicon electronic devices of about 50 nm in size can be fabricated in mass production.

GaAs is one of direct semiconductors for which a transition from the valence band to the conduction band does not require change of electron momentum. It can be used as a photodetector.

GaAs/AlGaAs heterostructures can make electrons have very high mobility at low temperature. The high mobility lengthens the electrons' phase-breaking mean free path. Therefore, coherent transport can be observed in GaAs/AlGaAs devices of μm scale at low temperature.

Bulk CdS absorbs visual light of the yellow-green wavelength, and its resistivity decreases with increasing illumination. CdS can be used as a photodetector and window material in solar cells.

Another quantum well application is the *high electron mobility transistor*. Figure 3 shows schematic of the cross-section of a high electron mobility transistor and its conduction band profile. The impurities in the doped AlGaAs layer provide electrons to the undoped GaAs layer, and the space charges and excess electrons bend the conduction band as shown in Fig. 3(b). Therefore, a quantum well is formed at the boundary of the undoped AlGaAs and the undoped GaAs. Since an Si-based metal-oxide-semiconductor FET has a structure similar to

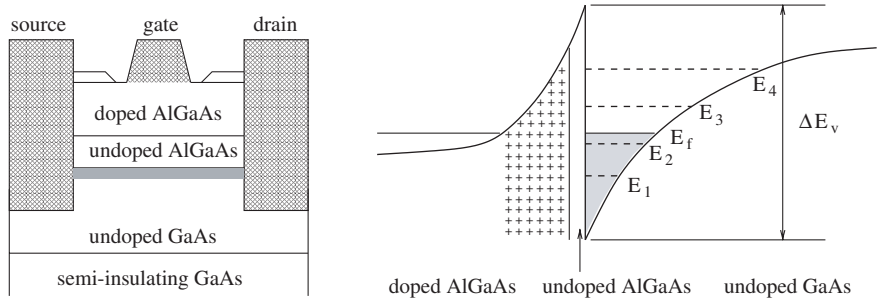

Fig. 3. A high electron mobility transistor based on the modulating doping: (a) cross-section and (b) conduction band profile of doped and undoped AlGaAs layers and undoped GaAs layer. The energy barrier of the conduction band is ΔE_c. The quantum well lies just below the undoped AlGaAs layer in (a), and lies to the right of the undoped AlGaAs in (b). The "bend" in the conduction band is caused by the excess electrons in the undoped GaAs layer and the spatial charges in the doped AlGaAs layer (as marked by "+"). The energy levels in the quantum well are discrete with regard to the dependence of variables in the longitudinal direction.

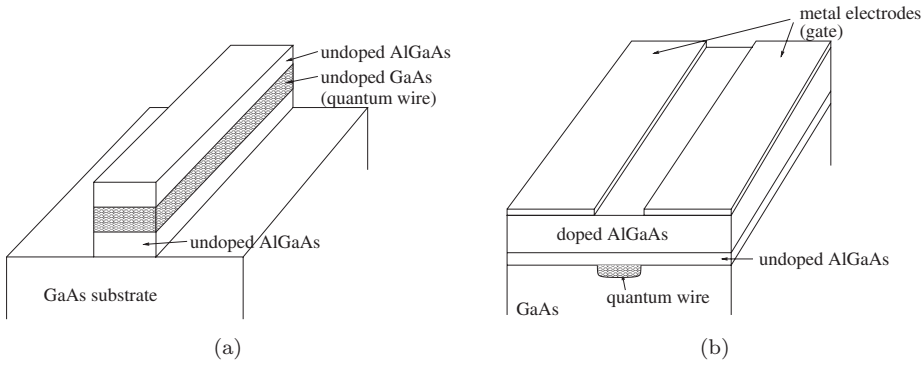

Fig. 4. A quantum wire fabricated from a quantum well structure: (a) etching of a portion of a quantum well structure and (b) deposition of metal gate on the top layer. The voltage applied to the metal gate depletes electrons underneath the gate, and electrons can gather underneath the place where the gate is not deposited.

high electron mobility transistor, quantum wells can be formed under certain conditions.

Figure 4 shows how quantum wires and QDs are fabricated from quantum wells in a top-down approach. One method is to remove part of a quantum well by etching, and the other is to apply an electric field above the quantum well. The former is used to confine the electron and hole at the same time, while the latter is to confine only an electron or a hole since the electric field prevents an electron (or a hole) from forming beneath the metal electrode. To etch the semiconductor material or to deposit the electrode, a nano-scale pattern has to be transferred by lithography. Various lithography technologies have been developed such as nano-imprinting,

AFM-STM lithography, dip-pen nanolithography, etc. Nevertheless, electron-beam lithography is currently the most widely used.

1.2. *QD-based single-electron devices and single-photon sources*

In Sec. 1.1, QD fabrication was discussed. In most of the proposals to be discussed in the next few sections, QD-based QCs are known to be single-electron devices. Recent advances in epitaxial growth technology have led to confinement of single electrons in semiconductor QDs. In QD-based "single-electron transistors" (SET), the position of a single electron governs the electrical conductance. However, the same factors that make single-electron detection simple also complicate construction of a QC based on sensing an electron's position. Charged electrons are easily de-localized by stray electric fields due to Coulomb interaction, and electrons placed in delicate entangled quantum states rapidly lose quantum coherence.[b] The localization of a single dot can be achieved either by advanced epitaxial growth techniques or by using novel optical manipulation techniques such as the near-field optical probe.

It was first predicted in 1938 that any two materials with different lattice constants would result in the formation of islands instead of flat layers beyond a critical thickness.[41] The growth of the first strain induced islands were reported by Goldstein *et al.*[18] in 1985, where InAs islands were formed on GaAs.[c] These islands can have sizes in the range of a few nanometers and can confine charge carriers both in the conduction band and in the valence band. Whatever we use the QD system for and whatever the fabrication technology we use, there will always be a statistical distribution of QD size and composition. This statistical distribution in turn produces inhomogeneous broadening of the QD optical response such as transition frequencies: this favors the distinction of one qubit from the others since the energy-domain discrimination is facile. Access to a specific qubit is achieved by positioning the excitation probe beam spot onto the desired location where a number of qubits with different frequencies can be accessed. Access to specific qubits can therefore be achieved by position selective addressing combined with frequency discrimination.

In addition, single-electron devices have a unique mechanism known as the *Coulomb blockade*, which is different from size quantization. Single electron tunneling occurs at an ultra-small junction. Electrons *cannot* pass through the ultra-small

[b] *Quantum coherence* refers to the property or condition of a quantum system whose constituents are *in-phase*, i.e. the various states that make up the overall wave-function have a well-defined, correlated phase relationship with one another as described by quantum mechanics. (This is to be contrasted with *quantum decoherence*, where the coherence of the process is lost.) The constituents in this paper are (mostly) electrons. But quantum particles such as electrons are identical and indistinguishable. The only way to tell them apart is via their "different identity cards" defined through *quantum numbers*. A system in quantum coherence is a linear combination (i.e. superposition) of eigenstates where each eigenstate is specified by a quantum number.

[c] This strain-induced-QD-growth method belongs to the bottom-up approach.

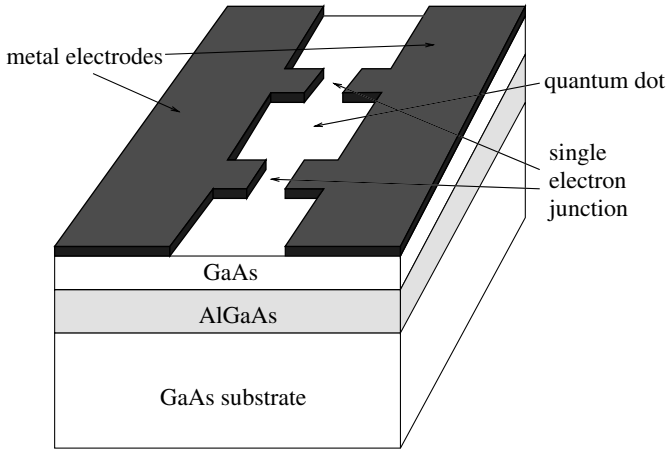

Fig. 5. A split-dual gate single-electron tunneling device. The voltage applied to the gate leads to single-electron junctions at the narrow channels and a quantum dot between the narrow channels. The capacitance of the junctions and the quantum dot size are dependent on the gate voltage.

junction due to electrostatic charging energy, which is the Coulomb blockade. Only when the electrostatic charging energy can be lowered by electron tunneling can a single electron then tunnel through the ultra-small junction, called a single electron junction. Quantitatively, when the capacitance of the junction is much smaller than $e^2/k_{\mathrm{B}}T$, where e is the absolute charge of electron, k_{B} is the Boltzmann constant and T is the temperature, single-electron tunneling is observed. Figure 5 shows a schematic of a single-electron tunneling device. It is built on a quantum well structure. There are two single electron junctions and one QD. If there is no electron in the QD, only a single electron can be at the QD by single electron tunneling. Various single-electron devices have been introduced such as the aforementioned SET, the single-electron box, and the single-electron turnstile.

Next, we consider the QD as a single photon generation source. Single photons were first generated in completely different kinds of quantum dots, colloidal quantum dots, which are synthesized in solutions.[28] These dots tend to suffer from blinking and bleaching; thus, improvements in their stability are required if practical devices are to be built with these dots. Their properties are currently closer to those of molecules than to those of Stranski–Krastanow QDs.[d] But because of the advantages of Stranski–Krastanow grown QD, most research has concentrated on epitaxially grown QD. However, one advantage of colloidal dots over epitaxially grown dots is that they still emit efficiently at room temperature.

[d]Briefly, Stranski–Krastanow QDs are grown by utilizing the strain caused by the lattice mismatch between the QD layer and the substrate during molecular beam epitaxy to form QD islands which are in the shape of a cylinder, pyramid, or truncated pyramid, with dimensions of about the exciton Bohr radius (see, for example, Refs. 4, 30, 31 and 46).

The recombination of an electron–hole pair leading to the emission of a photon with a specific energy is uniquely determined by the total charge configuration of the dot.[24] If a QD is optically pumped with a pulsed laser leading to the creation of several electron–hole pairs in the dot, then it is possible to spectrally isolate the single photon emitted by recombination of the last electron–hole pair.[17] QDs offer several advantages as sources for single photons. They have large oscillator strengths, narrow spectral linewidths, high photon yield, and excellent long-term stability. The materials used to make QDs are compatible with mature semiconductor technologies, allowing them to be further developed and integrated with other components. The usefulness of most QD single-photon sources, though, is limited by their low efficiencies. The dots radiate primarily into the high-index substrates in which they are embedded, and very few of the emitted photons can be collected. The source efficiency can be increased by placing a dot inside a microscopic optical cavity. Perhaps the most practical microcavities for this purpose are microscopic posts etched out of distributed-Bragg reflector (DBR) microcavities[39] (see Figs. 6 and 7). Light escaping from the fundamental mode of a micropost microcavity is well approximated by a Gaussian beam, and can thus be efficiently coupled into optical fibers, detectors, or other downstream optical components. Q as high as 10^4 together with a mode volume as small as 1.6 cubic optical wavelengths has been achieved. This translates to nearly 100% efficiency for a single-photon source.

1.3. *A simple QD for quantum computing*

We now illustrate a simple QD experiment as follows. Single quantum dots for quantum computation can be localized at the tip of strain induced self-assembled structures such as Stranski–Krastanow growth mode of GaN QDs grown on AlN

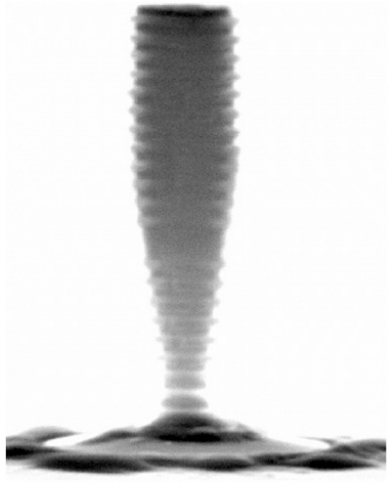

Fig. 6. Scanning-electron microscope image of a micropost microcavity with a top diameter of $0.6\,\mu$m and a height of $4.2\,\mu$m.

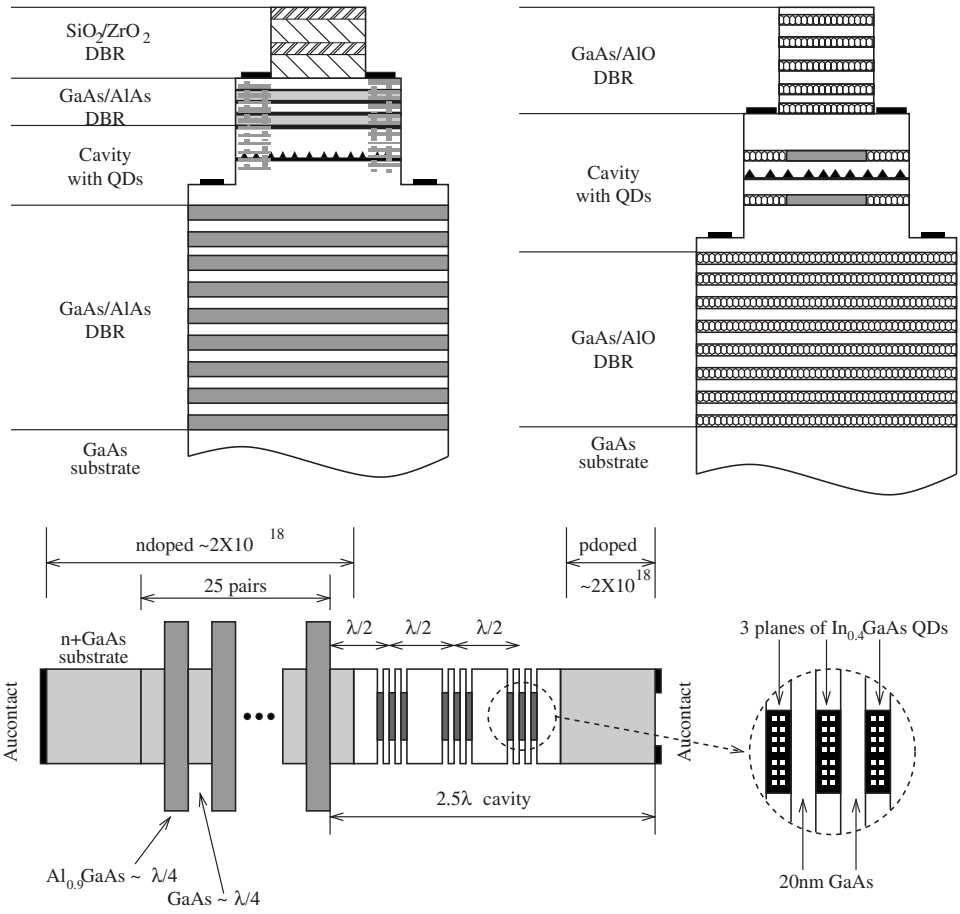

Fig. 7. QDs in a distributed-Bragg reflector, adapted from Refs. 21 and 22.

layers. A uniquely large hexagonal GaN pyramid (cf. Fig. 8) is self-assembled on the AlN cap on the surface of the GaN QD layers with a radius of curvature of no more than 300 nm. The faces of the pyramids are the $\{10\bar{1}\bar{1}\}$[e] planes as evidenced by the angle between the inclined edge and the base of the pyramid. The measured angle of around 58−60° is in good agreement with the calculated angle of 58.4° using the GaN lattice parameters of $c = 5.185\,\text{Å}$ and $a = 3.189\,\text{Å}$. The formation of the pyramids indicates that the $\{10\bar{1}\bar{1}\}$ surfaces are self-assembled preferentially compared to the $\{000\bar{1}\}$ surface. Thus, it can be inferred that $\{10\bar{1}\bar{1}\}$ surfaces have the lowest surface potential with respect to the self-assembly process. The tip of the pyramid is very sharp with a diameter measured to be less than 2 nm. It is

[e]This notation (and similar later) is called *Miller indices*, representing the plane on which the GaN lattices $\{10\bar{1}\bar{1}\}$ is grown (GaN is a wurtzite structure). A reference for Miller indices may be found in Ref. 48.

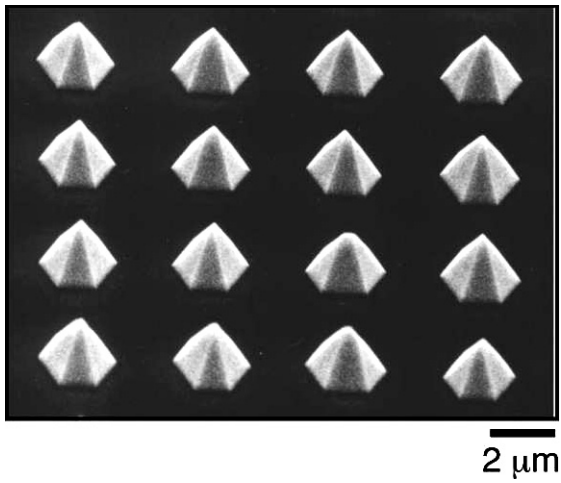

Fig. 8. GaN pyramids were selectively grown in 4 μm period and 2 μm square openings in a grid-like pattern. Three period of InGaN MQW structures (30 nm) were grown selectively on top of hexagonal GaN pyramids.

observed that GaN QDs are localized at the tip of the pyramid as demonstrated by the strong *excitonic* properties.

Near-field optical spectroscopy can be used for quantum computation as this probing technique is highly selective and has been utilized for exciting a single quantum dot system. Figure 9 shows the exciton emission from QDs localized at the tip of the pyramid. A comparison of the far-field and near-field spectrum shows that the emission from quantum confined states in a QD that are significantly blue-shifted compared to the bulk GaN states. In GaAs-based QDs, the linewidth of emission from single QDs has been observed to be less than a few μeV. In GaN-based QDs, the linewidth is broader due to larger longitudinal optical (LO) phonon scattering rate and electron effective mass, which leads to homogeneous broadening.

A periodic array of such GaN-based pyramids shown in Fig. 10 has been fabricated by Arakawa's group at University of Tokyo,[42] and can be used for quantum computation based on lateral coupling of the dots by using a near-field optical probe.

1.4. *Spintronics*

Spintronics is applicable to a QD-based QC, a proposal addressed in Sec. 3 of this paper. Spintronics is spin-based electronics with a spin degree of freedom added to the conventional charge-based electronic devices. Electrons have a half spin angular momentum, that is, there are two states of electron spin: spin-up and spin-down. Spintronics distinguishes spin-up electron current from spin-down electron current while charge-based electronics does not. Therefore, electron spin can be made to

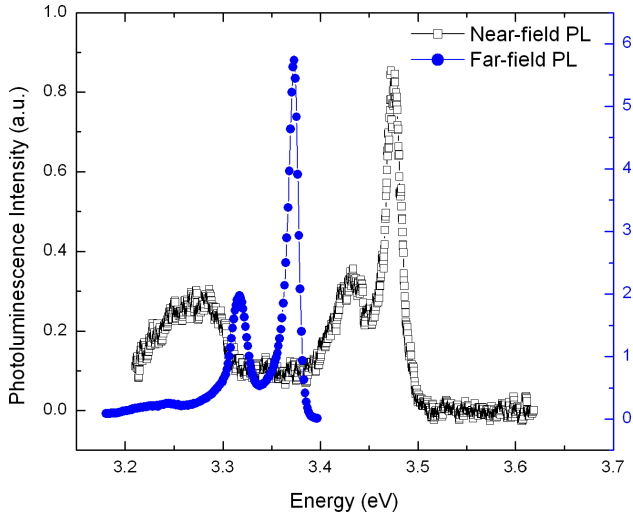

Fig. 9. Far-field and near-field photoluminescence (PL) spectrum from a GaN pyramid. The high energy emission at 3.48 eV observed in the near-field limit is from the QD localized at the top of the pyramid, whereas the far-field emission is dominated by the photoluminescence from *bulk* GaN states. The near-field PL spectrum signifies various energy levels (i.e. eigenstates) of the QD, which can be used to represent a single qubit for quantum computation.

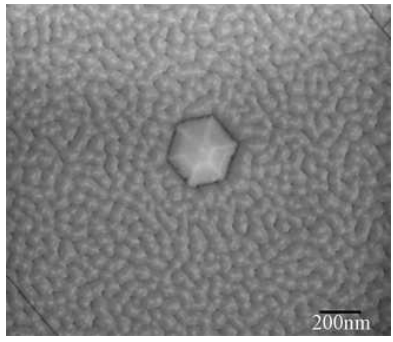

Fig. 10. SEM image showing the surface morphology and self-assembly of a hexagonal pyramid shape GaN structure with ~ 300 nm diameter.

carry information in spintronics. In 1988, it was reported in Ref. 3 that the resistance of a material is dependent on the magnetic moment alignment of the ferromagnetic layer, which is known as the *giant magnetoresistive* (GMR) effect. A simple GMR-based application is a spin valve as shown in Fig. 11. The top anti-ferromagnetic layer fixes the magnetic moment of the upper ferromagnetic layer. The lower ferromagnetic layer can change the direction of the magnetic moment in the presence of an external magnetic field. The resistance of the conductive layer varies with the external magnetic field due to the GMR effect. Spintronics is a type of device

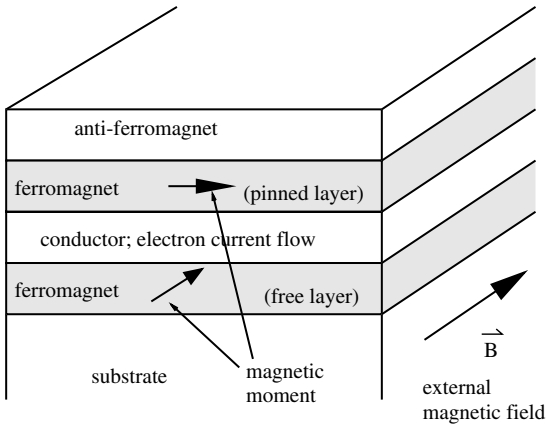

Fig. 11. A spin valve structure which is used to select desired electron spin current by an external magnetic field. The magnetization of the pinned layer is insensitive to the magnetic field, but that of the free layer can be changed. When the magnetic field aligns with the magnetic moments in the ferromagnetic layers, the resistance of the conductor reaches a minimum. When the magnetic field anti-aligns with the magnetic moments, the resistance reaches a maximum.

that merges electronics, photonics and magnetism. It is currently developing at a rapid pace.

1.5. *Three major designs of QD-based quantum gates*

QD designs allow for tunable bandgaps through the choices of QD sizes, shapes and semiconductor materials. For quantum gate logic operations, as mentioned in the preceding paragraphs, one can utilize *energy levels*, *spins*, or *excitonic levels* of confined electrons in quantum dots. At present, there exist three major designs of QD-based QC:

(i) Sherwin, Imamoglu and Montroy[36]: employ an idea similar to a cavity-QED design[11,35] by trapping single electrons in QD microcavities;
(ii) Loss and DiVincenzo[27]: utilize electron spins and their interactions via the electromagnetic effect of tunneling;
(iii) Piermarocchi *et al.*[33]: use a design based on coherent optical control of two electron–hole pairs (called a *biexciton*) confined in a single QD. Efforts are being made to couple two of more QDs in order to make this design scalable.

1.6. *Universality of 1-bit and 2-bit gates in quantum computing*

The executions of computations in QC are premised on the universality of the quantum gate operations in the QC. We first recall the following universality result.

Theorem 1 (Universality of 1-bit and 2-bit quantum gates[8]). *Let $\mathcal{A}$ be the collection of all 1-bit unitary rotation gates $U_{\theta,\phi}$, where*

$$U_{\theta,\phi} \equiv \begin{bmatrix} \cos\theta & -ie^{-i\phi}\sin\theta \\ -ie^{i\phi}\sin\theta & \cos\theta \end{bmatrix}, \quad 0 \le \theta, \ \ \phi \le 2\pi. \tag{1.1}$$

This collection $\mathcal{A}$, together with any single 2-bit gate V satisfying

$$V|xy\rangle \neq (S_1|x\rangle) \otimes (T_1|y\rangle), \quad V|xy\rangle \neq (S_2|y\rangle) \otimes (T_2|x\rangle); \qquad x, y \in \{0, 1\}, \tag{1.2}$$

for any 1-bit gates S_1, S_2, T_1 and T_2, constitute universal quantum gates for quantum computing. That is, any n-qubit quantum operation (as representable by a $2^n \times 2^n$ unitary matrix) can be achieved by a concatenation of such 1-bit gates $U_{\theta,\phi}$ and 2-bit gates V.

Therefore, in order to ensure universality, it is sufficient to have all the 1-bit gates $U_{\theta,\phi}$ in (1.1), plus any single 2-bit gate satisfying (1.2). These gates are derived from applying laser coherent control pulses and/or tunneling voltage gates in QDs. In the next few sections, we will provide the physical background and the mathematical equation governing these QD systems.

1.7. *Organization of the paper*

This paper is organized as follows: In Sec. 2, we study the microcavity approach of Sherwin *et al.*[36] In Sec. 3, we show the "spintronics" model following Loss and DiVincenzo.[27] In Sec. 4, we describe the biexciton model of Sham *et al.*[33] In each section, issues related to decoherence and measurement will also be discussed.

We should note that in addition to the three major proposals (i)–(iii) described in Sec. 1.5, many researchers have proposed QD-based entanglement schemes which can work as universal quantum gates. We apologize that we cannot cite all such schemes exhaustively here due to our limited knowledge and resources.

Another different application of QDs to computing, called the *quantum dot cellular automata* (QCA) approach, utilizes special properties of quantum decoherence in QDs to construct electronic logic gates. Information concerning QCA may be found on the Web.[54] A good expository reference may be found in Ref. 46.

2. Electrons in QDs Microcavity

The QC proposed by Sherwin *et al.*,[36] is a collection of QDs contained in a 3D microcavity. Each QD contains exactly one electron. The two lowest electronic states are used to encode $|0\rangle$ and $|1\rangle$, respectively. The third energy level $|2\rangle$, as an auxiliary state, is utilized to perform the conditional phase shift

operation; nevertheless, it does not directly encode any information. In addition, each QD is addressed by a pair of gate electrodes. Voltage pulses can be applied to control the energy levels of the QD via the Stark effect,[f] in particular, the energies E_{01} and E_{02} of the 0–1 and 0–2 transitions. The microcavity has a fundamental resonance with frequency ω_c. There is also a continuous-wave laser with a fixed frequency ω_l (different from ω_c) through one side of the cavity. The key technique to manipulate the state of the QD is to tune E_{01} and E_{02} with appropriate voltage pulses (through the gate electrodes) such that resonances with $\hbar\omega_c$, $\hbar\omega_l$, and $\hbar\omega_l + \hbar\omega_c$ are achieved. Coupling of different QDs is done via microcavity mode photons acting as the data bus. See the schematic in Fig. 12. Here, the QD configuration is similar to the QD in DBR microcavities in Sec. 1.2. The difference is that we use the cavity-mode photon confined in the cavity to communicate back and forth between QDs, while in the application of Sec. 1.2, the emphasis was to enhance the efficiency of generating cavity-mode photons emitted from the DBR microcavities for utilization by downstream optical devices.

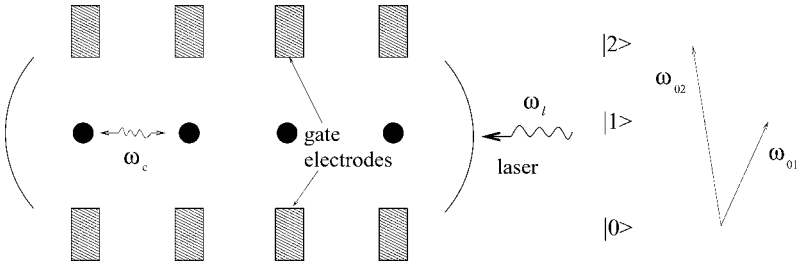

Fig. 12. The black dots represent the locations of QDs where the electrons are confined. The cavity photon with frequency ω_c serves as the data bus to couple two QDs. The figure on the right describes the three lowest energy levels utilized to perform qubit operations. The transition energies from $|0\rangle$ to $|1\rangle$ and $|0\rangle$ to $|2\rangle$ are given by $\hbar\omega_{01}$ and $\hbar\omega_{02}$, respectively, which can be tuned by the voltage pulse e.

[f]The Stark effect, discovered in 1913 by J. Stark, is the splitting of a spectral line into several components in the presence of an electric field. This splitting is called a Stark shift. The electric field may be externally applied, but in many cases it is an internal field caused by the neighboring ions or atoms. The effect is due to the interaction between the electric dipole moment of an electron with the electric field.

For semiconductor material, research on electroabsorption effects near the semiconductor band edges dates back to the 1950s. These include the interband photon-assisted tunneling or Franz–Keldysh effects[16] and exciton absorption effects.[14] With the appearance of quantum-confined structures, the optical absorption in quantum wells or QDs has been found to exhibit a dramatic change through exciton effects with an applied external electric field. This is caused by the so-called Quantum Confined Stark Effect (QCSE),[29] which led to the development of integrated electroabsorption devices at room temperature.

We may write down the following Hamiltonian to describe a QD interacting with cavity photons and laser fields:

$$\begin{aligned} H = {} & \hbar\omega_c \hat{a}_c^+ \hat{a}_c + E_{10}(e)\hat{\sigma}_{11} + E_{20}(e)\hat{\sigma}_{22} + \underbrace{\hbar g_{01}(e)\{\hat{a}_c^+ \hat{\sigma}_{01} + \sigma_{10}\hat{a}_c\}}_{\mathcal{J}_1} \\ & + \underbrace{\hbar\Omega_{l,01}(e)\{\hat{\sigma}_{01}e^{i\omega_l t} + \hat{\sigma}_{10}e^{-i\omega_l t}\}}_{\mathcal{J}_2} \\ & + \underbrace{\hbar g_{12}(e)\{\hat{a}_c^+ \hat{\sigma}_{12} + \hat{\sigma}_{12}\hat{a}_c\} + \hbar\Omega_{l,12}(e)\{\hat{a}_c^+ \hat{\sigma}_{12}e^{i\omega_l t} + \hat{\sigma}_{21}\hat{a}_c e^{-i\omega_l t}\}}_{\mathcal{J}_3}, \end{aligned} \tag{2.1}$$

where $\hat{a}_c$ is the cavity mode annihilation operator, g_{ij} are the vacuum Rabi frequencies, $\hat{\sigma}_{ij} = |i\rangle\langle j|$ for $i, j \in \{0, 1, 2\}$ are the transition operators, and e is the voltage pulse. Let e_c, e_l, and e_{l+c} be the proper heights of e such that $E_{10}(e_c) = \hbar\omega_c$, $E_{10}(e_\ell) = \hbar\omega_l$, and $E_{20}(e_{\ell+c}) = \hbar\omega_l + \hbar\omega_c$, respectively. The energies of the cavity mode photon, $\hbar\omega_c$, and the laser photon, $\hbar\omega_l$, should be sufficiently separated in order to have a satisfactory resonance performance. Typically, $\hbar\omega_c$ is 11.5 meV, and $\hbar\omega_l$ is 15 meV. The different effects of applying voltage pulses $e \approx e_c$, e_l, and e_{l+c} can be explained from this Hamiltonian. The meanings of individual terms in (2.1) are explained in Box 1.

There are a total of 11 terms in the Hamiltonian H in (2.1). Their origins can be explained as follows:

(i) The first three terms are called the *unperturbed Hamiltonian*, i.e. the Hamiltonian without interaction, where $\hbar\omega_c \hat{a}_c^+ a_c$ represents the energy of the cavity, and $E_{10}(e)\hat{\sigma}_{11} + E_{20}(e)\hat{\sigma}_{22}$ represents the energy of the three-level atom. Note that $E_{10}(e) = \hbar\omega_{01}$ and $E_{20}(e) = \hbar\omega_{02}$. (For the sake of simplicity, the vacuum energy of the cavity is omitted as it is a constant, and the energy of the atom at level $|0\rangle$ is taken to be 0.)

Interaction Terms: $\mathcal{J}_1, \mathcal{J}_2$ and $\mathcal{J}_3$:

(ii) The interaction between the atom and the cavity between the two levels $|0\rangle$ and $|1\rangle$ is modeled by $\mathcal{J}_1$. The single-mode cavity field stimulates a Rabi oscillation between $|0\rangle$ and $|1\rangle$, where $g_{01}(e)$ is the vacuum Rabi frequency. Term $\hat{a}_c^+ \hat{\sigma}_{01}$ describes the transition process when the atom jumps from $|1\rangle$ to $|0\rangle$ and a cavity photon is created, while $\hat{\sigma}_{01}\hat{a}_c$ describes the reverse process.

(iii) $\mathcal{J}_2$ contains the laser–atom interaction terms in a semi-classical form, where the electric field is not quantized (as the electric field induced by the laser is strong), with $\Omega_{\ell,01}$ as the Rabi frequency.

(iv) $\mathcal{J}_3$ is a combination of the effects of $\mathcal{J}_1$ and $\mathcal{J}_2$, except that it now describes the transition between levels $|0\rangle$ and $|2\rangle$.

Box 1. Meanings of the terms in the Hamiltonian (2.1).

In order to simplify the analysis of these three primary resonant cases, we have adopted the following assumptions:

(i) The time durations for the rise and fall of the voltage pulses e are relatively short, so that ideal heights are quickly reached to ensure that the targeted resonances dominate the overall state vector evolution.
(ii) The changes to the Hamiltonian H by the voltage pulses e is adiabatic, so that unwanted transitions between $|0\rangle$ and $|1\rangle$ induced by ramping electric fields are minimized.
(iii) The AC Stark shifts in the energy levels of the QD caused by the laser field are neglected.
(iv) The effect from the terms which do not satisfy resonance conditions is also neglected.

2.1. *Resonance, 1-bit and CNOT gates*

The details of the three primary resonant cases for (2.1) are:

(i) $e \approx e_c$: The first interaction term, $\hat{H}_1 = \hbar g_{01}(e)\{\hat{a}_c^+ \hat{\sigma}_{01} + \sigma_{10}\hat{a}_c\}$ in H [cf. the term $\mathcal{J}_1$ in (2.1)] dominates because of the resonance at $\omega_{10}(e) \approx \omega_c$. If the QD is in state $|1\rangle$ or if there is one photon in the cavity, i.e. the cavity state is $|1\rangle_c$, the qubit will undergo vacuum Rabi oscillations with frequency g_{01}:

$$|0\rangle|1\rangle_c \to \cos(g_{01}t)|0\rangle|1\rangle_c - ie^{i\phi}\sin(g_{01}t)|1\rangle|0\rangle_c, \tag{2.2}$$

$$|1\rangle|0\rangle_c \to \cos(g_{01}t)|1\rangle|0\rangle_c - ie^{-i\phi}\sin(g_{01}t)|0\rangle|1\rangle_c, \tag{2.3}$$

where $\phi = 0$. The above defines a rotation between state vectors $|0\rangle|1\rangle$ and $|1\rangle|0\rangle$, which is very similar to the 1-bit gate (1.1). We denote it as $U^{(1)}_{\theta,\phi} \equiv U_{\theta,\phi}(|0\rangle|1\rangle, |1\rangle|0\rangle)$ with $\theta = g_{01}t$, with $\phi = 0$.

(ii) $e \approx e_l$: The second interaction term, $\hat{H}_2 = \hbar\Omega_{l,01}(e)\{\hat{\sigma}_{01}e^{i\omega_l t} + \hat{\sigma}_{10}e^{-i\omega_l t}\}$ in H [cf. the term $\mathcal{J}_2$ in (2.1)] dominates. The state vector will rotate between $|0\rangle$ and $|1\rangle$ with Rabi frequency $\Omega_{l,01}$. We denote it as $U^{(2)}_{\theta,\phi} \equiv U_{\theta,\phi}(|0\rangle, |1\rangle)$ with $\theta = \Omega_{l,01}t$:

$$|0\rangle \to \cos(\Omega_{l,01}t)|0\rangle - ie^{i\phi}\sin(\Omega_{l,01}t)|1\rangle, \tag{2.4}$$

$$|1\rangle \to \cos(\Omega_{l,01}t)|1\rangle - ie^{-i\phi}\sin(\Omega_{l,01}t)|0\rangle. \tag{2.5}$$

(iii) $e \approx e_{l+c}$: The Rabi oscillation between $|0\rangle$ and $|2\rangle$ involving both cavity and laser photons will dominate the resonance behavior. From the $\mathcal{J}_3$ term in (2.1), after reduction we obtain the following effective Hamiltonian to describe these two-photon processes:

$$H_2 = \hbar\tilde{\Omega}(e)\{\hat{a}_c^+ \hat{\sigma}_{02}e^{i\omega_l t} + \hat{\sigma}_{20}\hat{a}_c e^{-i\omega_l t}\}. \tag{2.6}$$

If the cavity contains one photon, i.e. in state $|1\rangle_c$ and the QD is in state $|0\rangle$, then it rotates between $|0\rangle$ and $|2\rangle$ with frequency $\tilde{\Omega}(e_{l+c})$. We denote it as

$U^{(3)}_{\theta,\phi} \equiv U_{\theta,\phi}(|0\rangle, |2\rangle)$ with $\theta = \hat{\Omega}(e_{l+c})t$:

$$|0\rangle \to \cos(\tilde{\Omega}(e_{l+c})t)|0\rangle - ie^{i\phi}\sin(\tilde{\Omega}(e_{l+c})t)|2\rangle, \tag{2.7}$$

$$|2\rangle \to \cos(\tilde{\Omega}(e_{l+c})t)|2\rangle - ie^{-i\phi}\sin(\tilde{\Omega}(e_{l+c})t)|0\rangle. \tag{2.8}$$

Let us now address how to implement the CNOT (Controlled-NOT) gate in such a system. With respect to the ordered basis $\{|00\rangle, |01\rangle, |10\rangle, |11\rangle\}$, the matrix representation of the CNOT gate is

$$\begin{bmatrix} 1 & 0 & 0 & 0 \\ 0 & 1 & 0 & 0 \\ 0 & 0 & 0 & 1 \\ 0 & 0 & 1 & 0 \end{bmatrix}.$$

This task is achieved by first constructing the conditional phase shift $|00\rangle \to |00\rangle$, $|01\rangle \to |01\rangle$, $|10\rangle \to |10\rangle$, and $|11\rangle \to -|11\rangle$. The procedure is described in the following (by starting with a cavity with no photons):

(i) Apply a "π" pulse with height e_c and duration $\pi/(2g_{01})$ on the control bit. This pulse implements the rotation $U_{\pi/2,\pi}(|0\rangle|1\rangle, |1\rangle|0\rangle) = \begin{bmatrix} 0 & i \\ i & 0 \end{bmatrix}$, where a negative sign representing a global phase is omitted.

(ii) Apply a "2π" pulse with height e_{l+c}, phase 0, and duration $\pi/\tilde{\Omega}(e_{l+c})$ on the target bit. This pulse implements the rotation $U_{\pi,0}(|0\rangle, |2\rangle) = \begin{bmatrix} -1 & 0 \\ 0 & -1 \end{bmatrix}$.

(iii) Apply a "π" pulse with height e_c and duration $\pi/(2g_{01})$ on the control bit. Again, this pulse implements the rotation $U_{\pi/2,\pi}(|0\rangle|1\rangle, |1\rangle|0\rangle) = \begin{bmatrix} 0 & i \\ i & 0 \end{bmatrix}$.

These three steps will yield the quantum phase gate

$$Q_\pi = Q_\eta|_{\eta=\pi} \equiv \begin{bmatrix} 1 & 0 & 0 & 0 \\ 0 & 1 & 0 & 0 \\ 0 & 0 & 1 & 0 \\ 0 & 0 & 0 & e^{i\eta} \end{bmatrix}\Bigg|_{\eta=\pi}.$$

Theorem 2. *The above procedure implements the desired conditional phase shift to achieve the quantum phase gate Q_π.*

Proof. Following the previous discussion, we can derive the system states after each operation, starting from different initial states. The composite operation is $U^{(1)}_{\pi/2,\pi}U^{(3)}_{\pi,0}U^{(1)}_{\pi/2,\pi}$:

$$|00\rangle|0\rangle_c \to |00\rangle|0\rangle_c \to |00\rangle|0\rangle_c \to |00\rangle|0\rangle_c, \tag{2.9}$$

$$|01\rangle|0\rangle_c \to |01\rangle|0\rangle_c \to |01\rangle|0\rangle_c \to |01\rangle|0\rangle_c, \tag{2.10}$$

$$|10\rangle|0\rangle_c \to i|00\rangle|1\rangle_c \to -i|00\rangle|1\rangle_c \to |10\rangle|0\rangle_c, \tag{2.11}$$

$$|11\rangle|0\rangle_c \to i|01\rangle|1\rangle_c \to i|01\rangle|1\rangle_c \to -|11\rangle|0\rangle_c. \tag{2.12}$$

Ignoring the cavity bit $|0\rangle_c$, we have realized the conditional phase shift Q_π on two QDs.

This quantum phase gate Q_π satisfies (1.2) and is, therefore, a universal 2-bit gate. From Q_π, we can easily derive the CNOT gate by applying voltage pulses with height e_l, utilizing two more "$\frac{\pi}{2}$" and "$\frac{3\pi}{2}$" pulses with duration $\frac{\pi}{4\Omega_{l,01}}$ and $\frac{3\pi}{4\Omega_{l,01}}$, and phase $-\frac{\pi}{2}$, i.e.

$$\text{CNOT} = U^{(2)}_{3\pi/4,-\pi/2} Q_\pi U^{(2)}_{3\pi/4,-\pi/2}. \tag{2.13}$$

2.2. *Decoherence and measurement*

Decoherence as well as dissipation are major problems in the physical implementation of quantum computers. Any realistic quantum computer will have some interaction with its environment, which causes decoherence (decay of the off-diagonal elements of the reduced density matrix) and dissipation (change of populations of the reduced density matrix).[23] Because the data is encoded in the electronic states and the coupling of different QDs is carried out via microcavity mode photons in this QD scheme, decoherence of both electronic states and cavity photons must be considered. There are many interactions which may cause decoherence. Some of them come from devices' imperfections, which can be minimized by precision engineering. Examples of imperfections include the emission of freely propagating photons, interactions with the fluctuations in the potentials of the gate electrodes, and inhomogeneity of QDs. These problems can be tackled by using very high quality cavities, making the gate electrodes out of a superconductor, and individual calibration of each QD. Also, though the cavity photon loss — a dissipation effect — is inevitable in the long run, we can extend the lifetime of a cavity photon by using cavities made from materials such as ultrapure Si. However, there are other sources of decoherence which are more "essential" and hard to get rid of, such as the relaxation of an electron from state $|1\rangle$ to $|0\rangle$ by emission of an acoustic phonon, and the "pure dephasing" of electronic states by the interaction with acoustic phonons. If we assume that these are the dominant source of decoherence, it is estimated that within the decoherence time several thousands of CNOT operations can be safely performed. Nevertheless, limited by the technological complexity and lack of experimental results, accurate conclusions about the decoherence in this scheme still remain to be drawn.

The final stage of the quantum computing process is the readout of the states of the qubits. A tunable antenna-coupled intersubband terahertz (TACIT) photon detector is proposed for this task. Terahertz photons with frequencies close to the absorption frequency of the TACIT detector are efficiently detected. The absorption frequency can be tuned via the Stark effect similar to the way the transition energies of QDs are tuned. At the readout stage, we can tune this frequency to the fundamental resonance frequency ω_c of the cavity. Under the cavity resonance, if the qubit is in state $|1\rangle$, it will undergo Rabi oscillation with frequency g_{01} and emit a photon at time $\frac{\pi}{2g_{01}}$, which is immediately detected; otherwise, no photon will be seen. This way we can deduce whether the original state of the QD is $|0\rangle$ or $|1\rangle$.

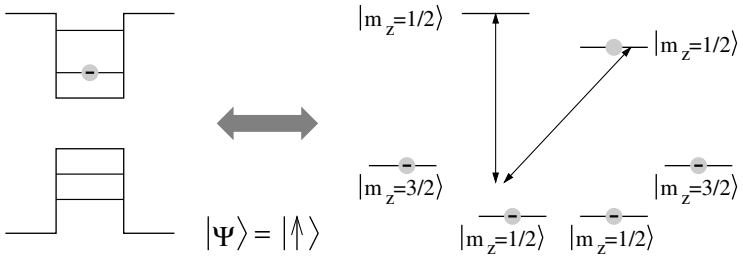

Fig. 13. Schematic for achieving qubits in multi-level QDs using electron-spin orbits.

3. Coupled Electron Spins in an Array of QDs

3.1. *Electron spin*

The electron spin is a "natural" representation of a qubit since it comprises exactly two levels. Unlike charge (energy-level) states in an atom or QD, there are no additional degrees of freedom into which the system could "leak." Another great advantage of spins as compared to charge qubits is that in typical semiconductor materials like GaAs or Si, the time over which the spin of a conduction-band electron remains phase coherent can be several orders of magnitude longer than the corresponding charge decoherence times. Of course, these numbers have to be compared with the time it takes to perform an elementary gate operation. Even with this being considered, single spins seem to be very well suited as qubits. The transverse decoherence time T_2, which is most relevant in the context of quantum computing, is defined as the characteristic time over which a single spin which is initially prepared as a coherent superposition of "spin up" and "spin down" coherently precesses about an external magnetic field. The transverse dephasing time $T_2^* \leq T_2$ of an ensemble of spins in n-doped GaAs can exceed 100 ns, as demonstrated by optical measurements,[20] while switching times are estimated to be of the order of 10–100 ps. The longitudinal (energy) relaxation time T_1 determines how long it takes for a non-equilibrium spin configuration to relax to equilibrium. T_1 can be much longer than T_2 (and particularly long in confined structures), but while suppression of spin relaxation is necessary for quantum computation, it is not sufficient.

There are two main schemes for achieving qubits in QDs using electron spin:

(i) Single-qubit rotations. In principle, spin-flip Raman transitions could rotate the electron spin in $\tau_{\text{gate}} \sim 10\,\text{ps} \ll \tau_{\text{decoh}} \sim 1\,\mu\text{s}$.
(ii) Two-qubit gates — the real challenge in most schemes. In this case, the spin decoherence during gate operation is a problem.

Spintronics requires the fabrication of ferromagnetic nanostructures that at room temperature can transport spin-polarized carriers, and which can be assembled into addressable hierarchies on a macroscopic chip. Most efforts have been

directed towards the mixing of transition-metal atoms (such as Ni, Fe and Mn, which have permanent magnetic moments) into semiconductor devices based on periodic table group II–VI (such as CdS) or III-V (GaAs) compound semiconductors. Superstructures consisting of alternating ferromagnetic/diamagnetic, metallic/oxide thin films have also received attention; like spin valves, spin-polarized currents can be injected into them and transported. An all-electrically controlled QD array can be used for switching qubits.

Recently, a new class of diluted magnetic semiconductor based on the III–V system is being studied due to its large intrinsic magnetic dipole moment. Gd-doped GaN materials are reported to have a strong intrinsic spin dipole moment. The tunneling in QD-based diluted magnetic semiconductors can also be enhanced by using a nanoscale electrode on a diluted magnetic semiconductor system.

3.2. *The design due to Loss and DiVincenzo*

In this section, we study questions related to spintronics design.[27] The basics of the Loss and DiVincenzo scheme is quite mathematically elegant. For a linear array of QDs (see Fig. 14), a single electron is injected into each dot. The electron's spin up and down constitute a single qubit. Each QD is coupled with its (two) nearest neighbors through gated tunneling barriers. The overall Hamiltonian of the array of coupled QDs is given in[10]:

$$H = \sum_{j=1}^{n} \mu_B g_j(t) \boldsymbol{B}_j(t) \cdot \boldsymbol{S}_j + \sum_{1 \le j < k \le n} J_{jk}(t) \boldsymbol{S}_j \cdot \boldsymbol{S}_k, \tag{3.1}$$

where the first summation denotes the sum of energy due to the application of a magnetic field $\boldsymbol{B}_j$ to the electron spin at dot j, while the second denotes the interaction Hamiltonian through the tunneling effect of a gate voltage applied between the dots, and $\boldsymbol{S}_j, \boldsymbol{S}_k$ are the spin of the electric charge quanta at, respectively, the jth and kth QD.

QDs themselves may be viewed as artificial atoms as both manifest similar behaviors. Coupled QDs, in this connection, may be considered to a certain extent as *artificial molecules*.[27] Thus, Burkard, Loss and DiVincenzo naturally applied the Heitler–London and Hund–Mulliken methods in molecular quantum chemistry

[g]The *Zeeman effect*, discovered by P. Zeeman in 1896, refers to the splitting of spectral lines by a magnetic field. For a quantum particle with spin lying in a magnetic field, interaction between its spin magnetic moment with the magnetic field causes its energy levels to split into several levels depending on the spin and the angular momentum quantum number. For QDs, the discrete energy levels, the transitions between those levels, and the associated spectral lines discussed so far have implicitly assumed that there are no magnetic fields influencing the QDs. If there are magnetic fields (due to the local magnetized layer) present, the electronic energy levels are split into a larger number of levels, and the spectral lines are also split.

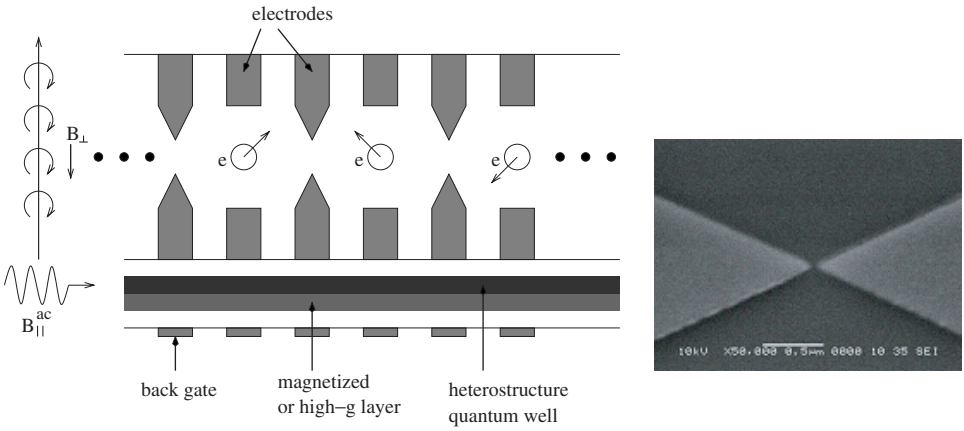

Fig. 14. (a) A linear array of laterally coupled QDs, as given in Burkard, Engel and Loss.[9] Each circle represents a QD, where the arrow represents the spin-$\frac{1}{2}$ ground state of the confined electron. The electrodes (dark gray) confine single electrons to the dot regions (circles). The electrons can be moved by electrical gating into the magnetized or high-magnetic dipole moment layer to produce locally different Zeeman splittings.[g] Alternatively, such local Zeeman fields can be produced by magnetic field gradients as, for example, produced by a current wire (indicated on the left of the dot-array). Since every dot-spin is subject to a different Zeeman splitting, the spins can be addressed individually, e.g. through ESR (electron-spin resonance) pulses of an additional in-plane magnetic AC field with the corresponding Larmor frequency (ω_{L}). Such mechanisms can be used for single-spin rotations and the initialization step. The exchange coupling between the dots is controlled by electrically lowering the tunnel barrier between the dots. (b) A nanofabricated bow-tie shaped electrode on Gd-doped GaN/AlN semiconductor QDs for spintronics.

to evaluate the "exchange energy" J, which in terms of our notation in (3.7) in Sec. 3.3, is

$$J = \frac{\hbar}{2}\omega(t).$$

J is a function of B, E and a, among others:

$$J = J(B, E, a), \tag{3.2}$$

where

B = the magnetic field strength,
E = the electric field strength, and
a = tunneling barrier height or, equivalently, inter-dot distance.

Varying these leads to, respectively, the effects of wave-function suppression, level detuning, and the suppression of tunneling between the dots.[27] The determination of $\omega(t)$ or, equivalently, J, is important. Technologically, the tailoring, design and implementation of the control pulse $\omega(t)$ are also perhaps the most challenging.

The coupling between two QDs consists of the usual Coulomb repulsion potential between the two electrons located within each dot and, in addition, a quartic potential

$$V(x,y) = \frac{m\omega_0^2}{2}\left[\frac{1}{4a^2}(x^2-a^2)^2 + y^2\right], \tag{3.3}$$

to model the effect of tunneling [see Fig. 15(b)]. Using the Heitler–London approach (likening the coupled QDs to the H_2 dimer), Burkard, Loss and DiVincenzo obtained

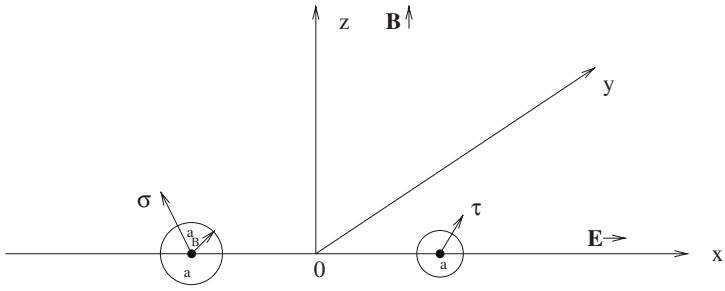

(a)

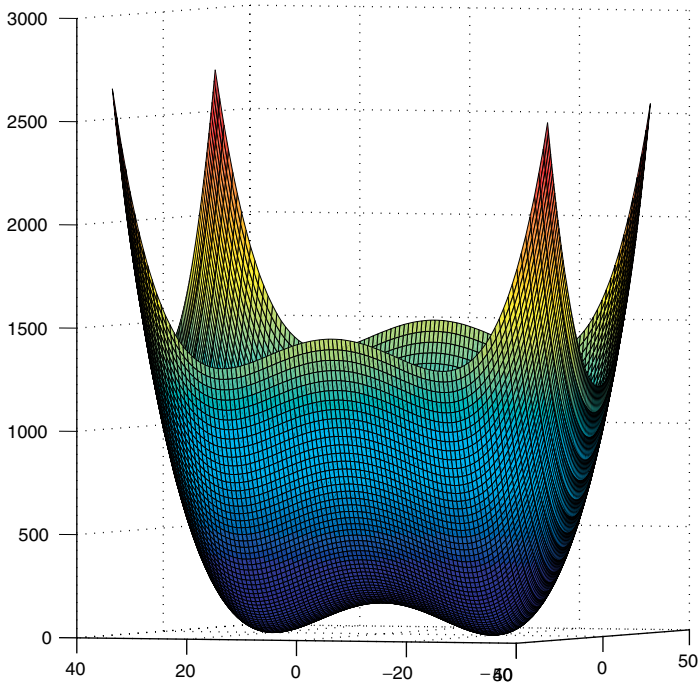

(b)

Fig. 15. (a) Geometry of the two identical coupled QDs. The two electrons are confined to the (x, y)-plane. Electron spins are denoted by $\boldsymbol{\sigma}$ and $\boldsymbol{\tau}$. (b) Profile of the quartic potential given by (3.3).

the exchange energy as

$$J = \frac{\hbar\omega_0}{\sinh(2d^2(2b - \frac{1}{b}))} \left[c\sqrt{b} \left\{ e^{-bd^2} I_0(bd^2) - e^{d^2(b-\frac{1}{b})} I_0 \left[d^2 \left(b - \frac{1}{b} \right) \right] \right\} + \frac{3}{4b}(1 + bd^2) + \frac{3}{2}\frac{1}{d^2} \left(\frac{eBa}{\hbar\omega_0} \right)^2 \right]. \quad (3.4)$$

The above result given in Ref. 10 is very commendable but its calculation is lengthy. Its derivations require special techniques and care, but details were not available in Ref. 10. We will fill in such technical mathematical details in Appendices A and B.

3.3. *Model of two identical laterally coupled QDs*

For the model given by Loss and DiVincenzo in Ref. 10, the underlying assumptions leading to the main result (3.4) are itemized as follows.

(i) The *geometry* of the two coupled dots is described in Fig. 15(a). The electron confinement is based on single GaAs heterostructure QDs formed in a 2DEG (two-dimensional electron gas). The directions of the electric and magnetic fields are indicated in Fig. 15(a), where

$$\boldsymbol{B} = B\boldsymbol{e}_z, \quad \text{due to the vector potential } \boldsymbol{A}(x, y, 0) = \frac{B}{2}(-y\boldsymbol{e}_x + x\boldsymbol{e}_y), \quad (3.5)$$

$$\boldsymbol{E} = E\boldsymbol{e}_x. \quad (3.6)$$

(ii) The quartic potential (3.3) for tunneling [see Fig. 15(b)] was motivated by experimental fact from Ref. 43 that the spectrum of single dots in GaAs is well described by a parabolic confinement potential, e.g. with $\hbar\omega_0 = 3\,\text{meV}$.[10,43] (The quartic potential (3.3) separates into two harmonic wells centered at $x = \pm a$.) The constant a, the half interdot distance, satisfies

$$a \gg a_B,$$

where $a_B = [\hbar/(m\omega_0)]^{1/2}$ is the effective Bohr radius of a single isolated harmonic well, and

μ_B is the Bohr magneton;
$g_j(t)$ is the effective g-factor;
$\boldsymbol{B}_j(t)$ is the applied magnetic field;
$J_{jk}(t)$ the time-dependent exchange constant (see Ref. 10 in references therein), with $J_{jk}(t) = 4t_{jk}^2(t)/u$, which is produced by the turning on and off of the tunneling matrix element $t_{ij}(t)$ between QDs i and j, with u being the charging energy of a single dot. Moreover, $J_{jk}(t) \equiv 0$ if $|j - k| > 1$.

Note that for

$$\boldsymbol{S}_j = \sigma_x^{(j)}\boldsymbol{e}_x + \sigma_y^{(j)}\boldsymbol{e}_y + \sigma_z^{(j)}\boldsymbol{e}_z, \quad j = 1, 2, \ldots, n,$$

and

$$\boldsymbol{B}_j(t) = b_x^{(j)}(t)\boldsymbol{e}_x + b_y^{(j)}(t)\boldsymbol{e}_y + b_z^{(j)}(t)\boldsymbol{e}_z, \quad j = 1, 2, \ldots, n,$$

where

$$\boldsymbol{e}_x = \begin{bmatrix} 1 \\ 0 \\ 0 \end{bmatrix}, \quad \boldsymbol{e}_y = \begin{bmatrix} 0 \\ 1 \\ 0 \end{bmatrix}, \quad \boldsymbol{e}_z = \begin{bmatrix} 0 \\ 0 \\ 1 \end{bmatrix},$$

and $\sigma_x^{(j)}, \sigma_y^{(j)}$ and $\sigma_z^{(j)}$ are the standard Pauli spin matrices (at dot j):

$$\sigma_x^{(j)} = \begin{bmatrix} 0 & 1 \\ 1 & 0 \end{bmatrix}, \quad \sigma_y^{(j)} = \begin{bmatrix} 0 & -i \\ i & 0 \end{bmatrix}, \quad \sigma_z^{(j)} = \begin{bmatrix} 1 & 0 \\ 0 & -1 \end{bmatrix}.$$

The dot products are defined by

$$\boldsymbol{S}_j \cdot \boldsymbol{S}_k = \sigma_x^{(j)}\sigma_x^{(k)} + \sigma_y^{(j)}\sigma_y^{(k)} + \sigma_z^{(j)}\sigma_z^{(k)},$$
$$\boldsymbol{B}_j(t) \cdot \boldsymbol{S}_j = b_x^{(j)}(t)\sigma_x^{(j)} + b_y^{(j)}(t)\sigma_y^{(j)} + b_z^{(j)}(t)\sigma_z^{(j)}.$$

From the universal quantum computing point of view, as the collection of 1-bit and 2-bit quantum gates are universal, it is sufficient to study a system with *only two coupled QDs*, whose Hamiltonian may now be written as[9,11]

$$H(t) \equiv \frac{\hbar}{2}[\boldsymbol{\Omega}_1(t) \cdot \boldsymbol{\sigma} + \boldsymbol{\Omega}_2(t) \cdot \boldsymbol{\tau} + \omega(t)\boldsymbol{\sigma} \cdot \boldsymbol{\tau}], \tag{3.7}$$

followed by rewriting the notation

$$\boldsymbol{S}_1 = \boldsymbol{\sigma}, \qquad \boldsymbol{S}_2 = \boldsymbol{\tau}; \quad \mu_B g_j(t)\boldsymbol{B}_j(t) = \frac{\hbar}{2}\boldsymbol{\Omega}_j(t), \quad j = 1, 2; \qquad J_{12}(t) = \frac{\hbar}{2}\omega(t).$$

The $\boldsymbol{\Omega}_1(t), \boldsymbol{\Omega}_2(t)$ and $\omega(t)$ are the *control pulses*. Thus, varying $\boldsymbol{\Omega}_1(t)$ and $\boldsymbol{\Omega}_2(t)$ will generate complete 1-bit Rabi-rotation gates for the first and second qubits, respectively.[11] However, in order to generate the *entangling* controlled-not (CNOT) gate or a quantum phase gate, both being 2-bit gates, the coupling term $\omega(t)\boldsymbol{\sigma} \cdot \boldsymbol{\tau}$ in (3.7) is indispensable. Therefore,

(iii) The Coulomb interaction between the two electrons is described by

$$C = \frac{e^2}{\kappa|\boldsymbol{r}_1 - \boldsymbol{r}_2|}, \quad \boldsymbol{r}_1 = x_1\boldsymbol{e}_x + y_1\boldsymbol{e}_y, \ \ \boldsymbol{r}_2 = x_2\boldsymbol{e}_x + y_2\boldsymbol{e}_y. \tag{3.8}$$

Here we assume that the screening length λ satisfies

$$\lambda/a \gg 1.$$

(iv) The ratio between the Zeeman splitting (due to the magnetic field $\boldsymbol{B}$) and the relevant orbital energies (see (v) below) is small for all values of B of interest here.

The spin-orbit effect can be neglected, as

$$H_{\text{spin-orbit}} = \left(\frac{\omega_0^2}{2mc^2}\right) \boldsymbol{L} \cdot \boldsymbol{S}$$
$$\left(c = \sqrt{\frac{\pi}{2}}\ \frac{e^2}{\kappa a_B}\frac{1}{\hbar\omega_0} \approx 2.4 \text{ for } \hbar\omega_0 = 3 \text{ meV},\ a_B = \sqrt{\frac{\hbar}{m\omega_0}}\right) \tag{3.9}$$

is of the magnetude

$$\frac{H_{\text{spin-orbit}}}{\hbar\omega_0} \approx 10^{-7}.$$

Consequently, the dephasing effects by potential or charge fluctuations can couple only to the charge of the electron, instead of the "holes."

Under conditions (1)–(4) above, the total orbital Hamiltonian of the coupled system may be given as

$$H_{\text{orb}} = h_1 + h_2 + C, \tag{3.10}$$

where

$$h_j = \frac{1}{2m}\left|\boldsymbol{p}_j - \frac{e}{c}\boldsymbol{A}(\boldsymbol{r}_j)\right|^2 + ex_jE + V(\boldsymbol{r}_j), \quad \text{for } j = 1, 2. \tag{3.11}$$

(v) Assume further the cryogenic condition $kT \ll \hbar\omega_0$, so we need only consider the two lowest orbital eigenstates of the orbital Hamiltonian H_{orb}, which are, respectively, the (symmetric) *spin-singlet* and the (antisymmetric) spin-triplet. A perturbation approximation then leads to the effective Heisenberg spin Hamiltonian

$$H_s = J\boldsymbol{S}_1 \cdot \boldsymbol{S}_2 \qquad [\text{cf. } J \text{ in (3.2)}],$$
$$J \equiv \epsilon_t - \epsilon_s = \text{the difference between the triplet and singlet energies.} \tag{3.12}$$

A self-contained account for the derivation of J involves rather technical mathematical analysis of the Fock–Darwin Hamiltonians and states, and clever simplifications of the various integrals in the exchange energy. We put together such work in Appendices A and B at the end of the paper.

The universality of the Loss–DiVincenzo QD quantum gates can now be presented. We first show how to choose the control pulse $\boldsymbol{\Omega}_1(t)$ in order to obtain the 1-bit unitary rotation gate $U_{\theta,\phi}$ in (1.1).

Theorem 3 (Ref. 11, pp. 111–112). *Let ϕ, $\theta \in [0, 2\pi]$ be given. Denote $\boldsymbol{e}(\phi) = \cos\phi\boldsymbol{e}_x + \sin\phi\boldsymbol{e}_y + 0\boldsymbol{e}_z$ for the given ϕ. Let $U_{1,\boldsymbol{\Omega}_1}(t)$ be the time evolution operator corresponding to the quantum system*

$$i\hbar\frac{\partial}{\partial t}|\psi(t)\rangle = H(t)|\psi(t)\rangle, \quad T > t > 0 \quad [\text{cf. } H(t) \text{ in (3.7)}], \tag{3.13}$$

where the pulses are chosen such that

$$\boldsymbol{\Omega}_1(t) = \Omega_1(t)\boldsymbol{e}(\phi), \quad \boldsymbol{\Omega}_2(t) = 0, \quad \omega(t) = 0, \qquad t \in [0, T], \tag{3.14}$$

with $\Omega_1(t)$ *satisfying*

$$\int_0^T \Omega_1(t)dt = 2\theta, \quad \text{for the given } \theta. \tag{3.15}$$

Then, the action of $U_{1,\boldsymbol{\Omega}_1}(t)$ *on the first qubit satisfies*

$$U_{1,\boldsymbol{\Omega}_1}(t) = U_{\theta,\phi}, \tag{3.16}$$

the 1*-bit unitary rotation gate* (1.1)*.*

Proof. We have

$$\begin{aligned} U_{\theta,\phi} &= \begin{bmatrix} \cos\theta & -ie^{-i\phi}\sin\theta \\ -ie^{i\phi}\sin\theta & \cos\theta \end{bmatrix} \\ &= \cos\theta\mathbf{1} - ie^{-i\phi}\sin\theta\left(\frac{\sigma_x - i\sigma_y}{2}\right) - ie^{i\phi}\sin\theta\left(\frac{\sigma_x - i\sigma_y}{2}\right) \\ &= \cos\theta\mathbf{1} - i\sin\theta\cos\phi\sigma_x - i\sin\theta\sin\phi\sigma_y \\ &= \cos\theta\mathbf{1} - i\sin\theta(\cos\phi\sigma_x + \sin\phi\sigma_y) \\ &= \cos\theta\mathbf{1} - i\sin\theta\boldsymbol{e}(\phi)\cdot\boldsymbol{\sigma} \\ &= e^{-i\theta\boldsymbol{e}(\phi)\cdot\boldsymbol{\sigma}}, \end{aligned} \tag{3.17}$$

noting that in the above, we have utilized the fact that the 2×2 matrix,

$$\boldsymbol{e}(\phi)\cdot\boldsymbol{\sigma} = \begin{bmatrix} 0 & \cos\phi - i\sin\phi \\ \cos\phi + i\sin\phi & 0 \end{bmatrix}, \tag{3.18}$$

satisfies $(\boldsymbol{e}(\phi)\cdot\boldsymbol{\sigma})^{2n} = \mathbf{1}$ for $n = 0, 1, 2, \ldots$, where $\mathbf{1}$ is the 2×2 identity matrix.

With the choices of the pulses as given in (3.14), we see that the second qubit remains steady in the time evolution of the system. The Hamiltonian is now

$$H_1(t) = \frac{\hbar}{2}\Omega_1(t)\boldsymbol{e}_1(\phi)\cdot\boldsymbol{\sigma}, \tag{3.19}$$

and acts only on the first qubit (where the subscript 1 of $\boldsymbol{e}_1(\phi)$ denotes that this is the vector $\boldsymbol{e}(\phi)$ for the first bit). Because $\Omega_1(t)$ is scalar-valued, we have

$$H_1(t_1)H_1(t_2) = H_1(t_2)H_1(t_1) \quad \text{for any } t_1, t_2 \in [0, T]. \tag{3.20}$$

Thus,

$$\begin{aligned} U_{1,\boldsymbol{\Omega}_1}(T) &= e^{-\frac{i}{2}\int_0^T \Omega_1(t)\boldsymbol{e}_1(\phi)\cdot\boldsymbol{\sigma}dt} \\ &= e^{\left[-\frac{i}{2}\int_0^T \Omega_1(t)dt\right]\boldsymbol{e}_1(\phi)\cdot\boldsymbol{\sigma}} \\ &= e^{-i\theta\boldsymbol{e}_1(\phi)\cdot\boldsymbol{\sigma}}, \qquad [\text{by (3.15)}] \end{aligned} \tag{3.21}$$

using (3.17).

We may define $U_{2,\mathbf{\Omega}_2}$ in a similar way as in Theorem 3.

Next, we derive the 2-bit quantum phase gate Q_π and the CNOT gate. This will be done through the square root of the swap gate $U_{\rm sw}$:

$$U_{\rm sw}(|ij\rangle) = |ji\rangle, \quad \text{for } i,j \in \{0,1\}. \tag{3.22}$$

Theorem 4 (Ref. 11, pp. 110–111). *Denote by $U(t)$ the time evolution operator for the quantum system (3.7) for the time duration $t \in [0,T]$. Choose $\mathbf{\Omega}_1(t) = \mathbf{\Omega}_2(t) = 0$ in (3.7) and let $\omega(t)$ therein satisty*

$$\int_0^T \omega(t)dt = \frac{\pi}{2}. \tag{3.23}$$

Then, we have $U(T) = -e^{\pi i/4}U_{\rm sw}$, i.e. $U(T)$ is the swapping gate (with a non-essential phase factor $-e^{\pi i/4}$.)

Proof. From assumptions, we now have

$$H(t) = \omega(t)\boldsymbol{\sigma}\cdot\boldsymbol{\tau}/2. \tag{3.24}$$

Since $\omega(t)$ is scalar-valued, we have the commutativity

$$H(t_1)H(t_2) = H(t_2)H(t_1), \quad \text{for any } t_1,t_2 \in [0,T]. \tag{3.25}$$

Therefore,

$$\begin{aligned} U(T) &= e^{-i\int_0^T H(t)dt/\hbar} = e^{\left[-\frac{i}{2}\int_0^T \omega(t)dt\right]\boldsymbol{\sigma}\cdot\boldsymbol{\tau}} \\ &= e^{-i\phi\boldsymbol{\sigma}\cdot\boldsymbol{\tau}} \qquad \left(\phi \equiv \frac{1}{2}\int_0^T \omega(t)dt\right) \\ &= \cos(\phi\boldsymbol{\sigma}\cdot\boldsymbol{\tau}) - i\sin(\phi\boldsymbol{\sigma}\cdot\boldsymbol{\tau}), \end{aligned} \tag{3.26}$$

where $e^{-i\phi\boldsymbol{\sigma}\cdot\boldsymbol{\tau}}$, $\cos(\phi\boldsymbol{\sigma}\cdot\boldsymbol{\tau})$ and $\sin(\phi\boldsymbol{\sigma}\cdot\boldsymbol{\tau})$ are 4×4 matrices. Since

$$\boldsymbol{\sigma}\cdot\boldsymbol{\tau} = \begin{bmatrix} 1 & 0 & 0 & 0 \\ 0 & -1 & 2 & 0 \\ 0 & 2 & -1 & 0 \\ 0 & 0 & 0 & 1 \end{bmatrix}$$

has a three-fold eigenvalue $+1$ (triplet) and a single eigenvalue (singlet) -3, the associated projection operators can easily be found to be

$$\begin{aligned} \boldsymbol{P}_1 &= \frac{1}{4}(3\mathbf{1} + \boldsymbol{\sigma}\cdot\boldsymbol{\tau}) \quad \text{and} \quad \boldsymbol{P}_2 = \frac{1}{4}(\mathbf{1} - \boldsymbol{\sigma}\cdot\boldsymbol{\tau}); \\ \boldsymbol{P}_j\boldsymbol{P}_k &= \begin{cases} 0, & j \neq k, \\ \boldsymbol{P}_j, & j = k. \end{cases} \end{aligned} \tag{3.27}$$

Thus, from (3.26) and (3.27), we obtain

$$U(T) = e^{-i\phi\boldsymbol{\sigma}\cdot\boldsymbol{\tau}} = e^{-i\phi}\cdot\frac{1}{4}(3\mathbf{1} + \boldsymbol{\sigma}\cdot\boldsymbol{\tau}) + e^{-3i\phi}\cdot\frac{1}{4}(\mathbf{1} - \boldsymbol{\sigma}\cdot\boldsymbol{\tau}). \tag{3.28}$$

With a little manipulation, (3.28) becomes

$$\begin{aligned} U(T) &= e^{i\phi}\left[\cos(2\phi)\mathbf{1} - i\sin(2\phi)\frac{\mathbf{1}+\boldsymbol{\sigma}\cdot\boldsymbol{\tau}}{2}\right] \\ &= e^{i\phi}[\cos(2\phi)\mathbf{1} - i\sin(2\phi)U_{\mathrm{sw}}], \end{aligned} \tag{3.29}$$

using the fact that

$$U_{\mathrm{sw}} = \begin{bmatrix} 1 & 0 & 0 & 0 \\ 0 & 0 & 1 & 0 \\ 0 & 1 & 0 & 0 \\ 0 & 0 & 0 & 1 \end{bmatrix} = \frac{1}{2}(\mathbf{1} + \boldsymbol{\sigma}\cdot\boldsymbol{\tau}).$$

Choosing $\phi = \pi/4$, we obtain the desired conclusion.

Corollary 1 (Ref. 11, pp. 110–111). *The square roots of the swapping gate* $U_{\mathrm{sw}}^{1/2}$ *are*

$$U_{\mathrm{sw}}^{1/2} = \frac{e^{\pm\pi i/4}}{\sqrt{2}}(\mathbf{1} \mp iU_{\mathrm{sw}}). \tag{3.30}$$

Proof. From (3.29), we first obtain

$$U_{\mathrm{sw}} = ie^{-\frac{\pi i}{4}}U(T). \tag{3.31}$$

Then, we use $\phi = \pm\pi/8$ in (3.29) to obtain

$$U_{\mathrm{sw}}^{1/2} = (ie^{-\frac{\pi i}{4}})^{1/2}e^{\pm\pi i/8}\left[\frac{1}{\sqrt{2}}(\mathbf{1} \mp iU_{\mathrm{sw}})\right], \tag{3.32}$$

and the desired conclusion. (Note that these two square roots of U_{sw} reflect the choices of $\sqrt{1} = 1$ and the square root of $-1 = \pm i$ for the square roots of the eigenvalues of U_{sw}.)

Corollary 2 (Ref. 11, p. 112). *The quantum phase gate* Q_π *is given by*

$$Q_\pi = (-i)U_{1,\boldsymbol{\Omega}_1^{(2)}}U_{2,\boldsymbol{\Omega}_2}U_{\mathrm{sw}}^{1/2}U_{1,\boldsymbol{\Omega}_1^{(1)}}U_{\mathrm{sw}}^{1/2}, \tag{3.34}$$

where

$$\begin{cases} \displaystyle\int \boldsymbol{\Omega}_1^{(1)}(t)\,dt = -\pi\boldsymbol{e}_{1z}, \\ \displaystyle\int \boldsymbol{\Omega}_1^{(2)}(t)\,dt = \pi\boldsymbol{e}_{1z}/2, \\ \displaystyle\int \boldsymbol{\Omega}_2(t)\,dt = -\pi\boldsymbol{e}_{2z}/2, \end{cases} \tag{3.35}$$

and $\boldsymbol{e}_{1z}, \boldsymbol{e}_{2z}$ *denote the* $\boldsymbol{e}_z$ *vector of, respectively, the first and the second qubit.*

Remark 2. In order to realize this succession of gates, only one of the $\mathbf{\Omega}(t)$ in (3.35) is nonzero at any given instant t, with the duration when $\mathbf{\Omega}_1^{(1)}(t) \neq 0$ earlier than that when $\mathbf{\Omega}_2(t) \neq 0$, and that when $\mathbf{\Omega}_1^{(2)}(t) \neq 0$ even later. Earliest is the period when $\omega(t) \neq 0$ for the first $U_{\rm sw}^{1/2}$, and another period when $\omega(t) \neq 0$ is intermediate between those when $\mathbf{\Omega}_1^{(1)}(t) \neq 0$ and $\mathbf{\Omega}_2(t) \neq 0$.

Proof. Define

$$U_{\rm XOR} \equiv e^{\frac{\pi i}{4}\sigma_z} e^{-\frac{\pi i}{4}\tau_z} U_{\rm sw}^{1/2} e^{i\frac{\pi}{2}\sigma_z} U_{\rm sw}^{1/2}, \tag{3.36}$$

with $U_{\rm sw}^{1/2} = \frac{e^{-\frac{\pi}{4}i}}{\sqrt{2}}(\mathbf{1}+iU_{\rm sw})$ chosen from (3.30). Then, it is straightforward to check that

$$\begin{aligned} &U_{\rm XOR}|00\rangle = |00\rangle(i), \quad U_{\rm XOR}|01\rangle = |01\rangle(i), \\ &U_{\rm XOR}|10\rangle = |10\rangle(i), \quad U_{\rm XOR}|11\rangle = |11\rangle(-i), \end{aligned} \tag{3.37}$$

so that

$$\begin{aligned} U_{\rm XOR} &= i(|00\rangle\langle 00| + |01\rangle\langle 01| + |10\rangle\langle 10| - |11\rangle\langle 11|) \\ &= iQ_\pi. \end{aligned} \tag{3.38}$$

From the quantum phase gate Q_π, we again obtain the CNOT gate as in (2.13).

As a final comment of this section, we note that the two QDs in coupling are assumed to be identical. However, the state-of-the-art of fabrication of QDs with uniform size and characteristics is far from being perfected with current technology. A more refined mathematical treatment for the modeling of two non-identical QDs in coupling is needed.

3.4. *More details of the QD arrangements: Laterally coupled and vertically coupled arrays*

The discussions so far in this section are geared toward laterally coupled QDs. Let us now give some details of QD array arrangement. In coupled QDs, there exists the combined action of the Coulomb interaction and the Pauli exclusion principle. Two coupled electrons in the absence of a magnetic field have a spin-singlet ground state, while the first excited state in the presence of strong Coulomb repulsion is a spin triplet (recall the discussions of singlet and triplet in the proof of Theorem 4). Higher excited states are separated from these two lowest states by an energy gap, given either by the Coulomb repulsion or the single-particle confinement. For lateral coupling, the dots are arranged in a plane, at a sufficiently small distance, say $2a$ [cf. (3.2)–(3.4)], such that the electrons can tunnel between the dots (for a lowered barrier) and an exchange interaction J between the two spins is produced. Lateral coupling amongst QDs lying in a single plane can be achieved by two different techniques: first, by controlling the material system, and

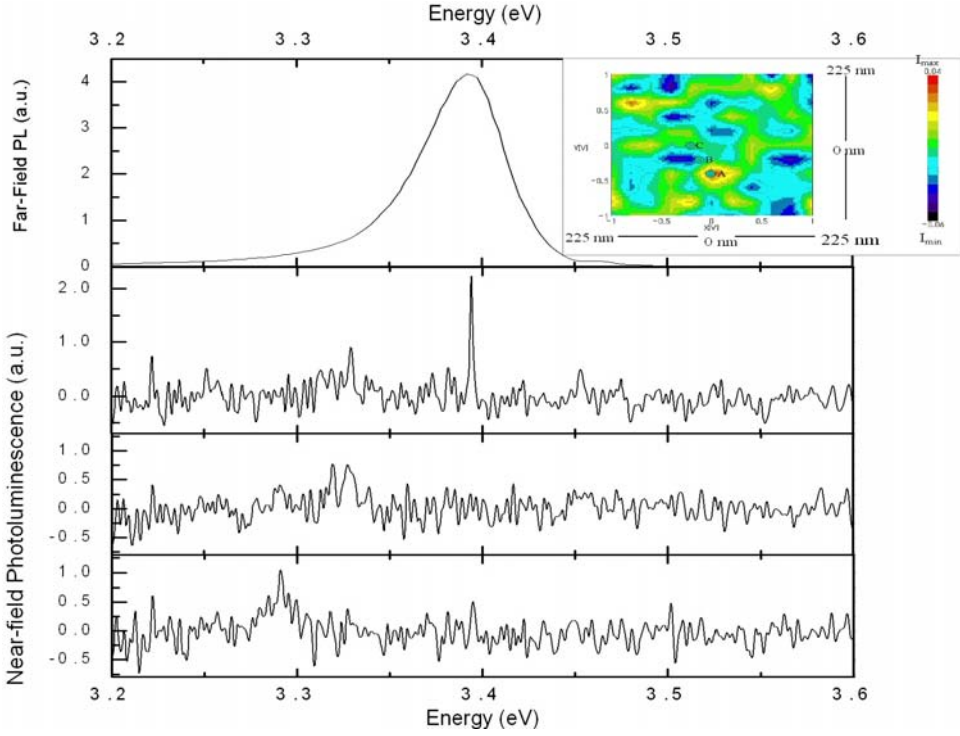

Fig. 16. Near-field photoluminescence emission from laterally coupled QDs.

then by having spatial correlation between adjoining dots that can lead to splitting of eigenstates within a single dot into symmetric and antisymmetric states; secondly, by using a near-field probe that can induce an electromagnetic coupling between neighboring QDs. Figure 16 shows a laterally coupled GaN/AlN single period QD system probed by near-field optical spectroscopy. In the absence of tunneling between the dots, we still might have direct Coulomb interaction left between the electrons. However, this has no effect on the spins (qubit) provided the spin-orbit coupling is sufficiently small, which is the case for s-wave electrons in III–V semiconductors with unbroken inversion symmetry (this would not be so for hole-doped systems since the hole has a much stronger spin-orbit coupling due to its p-wave character). Finally, the vanishing of J in (3.1) or (3.2) can be exploited for switching by applying a constant homogeneous magnetic field to an array of QDs to tune J to zero (or close to some other desirable value). Then, for switching J on and off, only a small gate pulse or a small local magnetic field is needed.

Figure 16(a) shows the far-field PL (photonluminescence) spectrum, which is broadband and includes an ensemble effect of the emission from various QDs. Figure 16(b) shows the emission from various regions A–C as mapped in spatial

PL map show above. The emissions from individual dots are observed from the narrow PL spectrum, some of which are inhomogeneously broadened due to lateral coupling. A greater control of laterally coupled QDs can be achieved by using patterned substrates so that the electrons in a confined QD can be controlled by tailoring the eigenfunction of the conduction subbands.[32]

The arrangement of vertically tunnel-coupled QDs has also been studied by Burkard, Loss, and DiVincenzo.[10] The mathematical modeling is quite similar to the laterally coupled case so we omit it here and refer the interested reader to Ref. 10. Neogi *et al.*[31] consider such a setup of the dots, which has been produced in multilayer self-assembled QDs as well as in etched mesa heterostructures.

To gain insight into the spatial variation of GaN QDs and quantum wells on the emission intensity and linewidth, cross-sectional transmission electron microscopy (TEM) was performed. Samples were processed in a dual-beam SEM/FIB[h] (FEI Nova 600) using a Ga ion-beam accelerating voltage of 5 kV, followed by examination in a Tecnai F20 analytical HRTEM.[i] A near vertical correlation of the GaN dots ~ 30 nm in width is observed from a STEM[j]-HAADF[k] image (not shown here), with some dot assemblies correlated at an angle slightly off vertical. It is also observed that the width of these dots and their period correspond to the surface texture observed in the SEM image (Fig. 10). An HRTEM image shown in Fig. 17 illustrates that 1.1–2 nm high GaN QD-like clusters are embedded in GaN/AlN quantum wall-like structures.

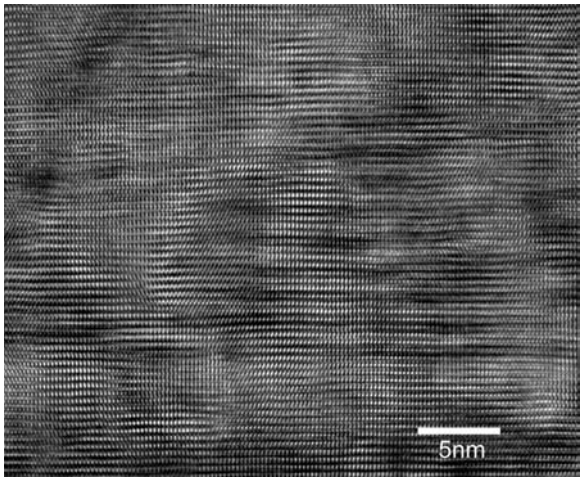

Fig. 17. HRTEM image showing $\langle 1-1-1-0 \rangle$ cross-section of stacked layers of GaN dots.

[h]SEM: scanning electron microscope; FIB: focused ion-beam.
[i]HRTEM: high-resolution transmission electron microscope.
[j]STEM: scanning transmission electron microscope.
[k]High-angle annular dark-field.

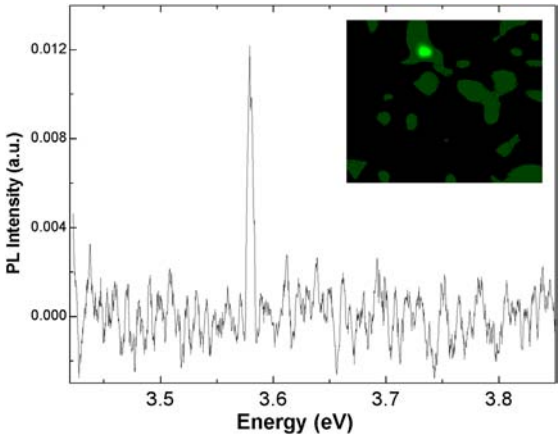

Fig. 18. Near-field emission from a single GaN/AlN QD excited by a He-Cd laser at 325 nm. The scanning area is 450 nm × 450 nm.

The vertical correlation provides a lower radiative recombination lifetime and higher emission efficiency due to tunneling via the vertically connected dots, especially in case of thin AlN spacer layers. Figure 18 shows strong emission from a single cluster of QDs from a 450 nm × 450 nm area.

Switching of the spin–spin coupling between dots of different size can be achieved by means of varying external electric and magnetic fields. The exchange interaction[1] is not only sensitive to the magnitude of the applied fields, but also to their direction. It has been predicted that an in-plane magnetic field $B_{\|}$ suppresses J exponentially; a perpendicular field in laterally coupled dots has the same effect. A perpendicular magnetic field $B_{\perp}$ reduces, on one hand, the exchange coupling between identically sized dots and, on the other hand, for different dot sizes: increasing $B_{\perp}$ amplifies the exchange coupling J until the electronic orbitals of the various QD are magnetically compressed to approximately the same size. A perpendicular electric field $E_{\perp}$ detunes the single-dot levels, and thus reduces the exchange coupling; the very same finding was made for laterally coupled dots and an in-plane electric field.[10]

3.5. *Decoherence and measurement*

The main source of decoherence for this model is environmental fluctuation. For electron spin, it is the fluctuation of the ambient magnetic field. This effect can be modeled as the linear interaction between the electron spin and the environment modeled as a set of harmonic oscillators (called a Caldeira–Leggett-type model).

[1]The exchange interaction is the "off-diagonal" effect of the Coulomb forces acting on two interacting particles (here, the two electrons and their spins in two neighboring QDs). This exchange interaction is characterized by the quantity J given in Appendix B.

For a two-spin system, the interaction Hamiltonian is $H_{\rm int} = \lambda \sum_{i=1,2} \boldsymbol{S}_i \cdot \boldsymbol{b}_i$, where $\boldsymbol{S}_i$ is the angular momentum of the electron spin and the jth component of $\boldsymbol{b}_i$, $b_i^j = \sum_\alpha g_\alpha^{ij}(a_{\alpha,ij}^+ + a_{\alpha,ij})$, is the fluctuating field. Here, $a_{\alpha,ij}^+$ and $a_{\alpha,ij}$ are, respectively, the creation and annihilation operators of the magnetic field with mode α, respectively, and g_α^{ij} is the amplitude. The unperturbed harmonic-oscillator Hamiltonian of the magnetic field can be written as $H_{\rm B} = \sum \omega_\alpha^{ij} a_{\alpha,ij}^+ a_{\alpha,ij} + \frac{1}{2}$, where the subscript "B" represents "bath," i.e. the environment, and ω_α^{ij} is the frequency of the mode α of the field. Interest is focused on the density matrix of the system, which is obtained by tracing the bath from the total density matrix $\bar{\rho}(t)$, $\rho(t) = {\rm Tr}_{\rm B}\bar{\rho}(t)$. The dynamics of $\bar{\rho}(t)$ satisfies the von Neumann equation

$$\frac{\partial \bar{\rho}(t)}{\partial t} = -i[H, \bar{\rho}(t)] = -i\mathcal{L}\bar{\rho}(t), \tag{3.39}$$

where H is the whole Hamiltonian including the unperturbed system Hamiltonian $H_{\rm s}$:

$$H = H_{\rm s} + H_{\rm int} + H_{\rm B}, \tag{3.40}$$

and $\mathcal{L}$ is the corresponding Liouvillian super operator.

A detailed computation of the effect of the decoherence on the quantum system when the swap gate or 1-bit rotation gate are applied is given in Ref. 27. That result shows that the decoherence time has an order of 1.4 ns while the time needed for one logic gate operation has an order of 25 ps, which is very satisfactory for quantum computation. The reference model used in the computation has an exchange constant $J = 80\,\mu$eV and the ambient magnetic fields are assumed to be at thermal equilibrium.

Measurement of a single spin in a QD is obviously difficult because of the weak signal and strong background noise. Elegant schemes are needed to overcome this difficulty. One could utilize a switchable tunneling with which the electron tunnels into a super-cooled paramagnetic dot (PM) before the measurement. Then, it nucleates a ferromagnetic domain whose magnetization can be measured by conventional methods. The fidelity of successful measurement with this method is expected to be about 75% when the magnetization in the upper hemisphere is interpreted as a spin-up state of the electron. Another scheme utilizes a switchable valve or barrier which is only transparent to electrons of the spin-up state. When a spin is to be measured, this switchable valve only lets the spin-up electron pass to another QD (called a measure dot). Then a nanoscale single-electron electrometer can be used to detect the presence of an electron in the measure dot. If an electron is found there, it is in the spin-up state; otherwise, it is in the spin-down state.

3.6. *New advances*

Recent advances in nanofabrication have greatly facilitated the development of spin-based devices. The accurate estimation of the QD size distribution in the nanoscale limit is critical to the optimization of the radiative emission rate, device design

and fabrication of integrated QD-based quantum computational structures. The focused ion-beam (FIB) lithography technique overcomes the diffraction-limited spot size occurring in convention photolithography. FIBs offer advantages over the conventional photo-processing technique in precision and fine resolution, and extends the capability of photoprocessing to the nanometer region. FIB-aided processing of semiconductor optoelectronic devices have facilitated progress recently in the areas of photoprocessing and photofabrication with a higher degree of precision and resolution.[2,45] The patterning and machining of electrodes with nanoscale resolution over QD structures in the FIB allows for the unique opportunity of simultaneously preparing cross-sectional TEM at sub-micron spatial resolutions.

We should also mention that many solid-state implementations for quantum computing have been proposed subsequently,[26] including superconducting qubits, nuclear spins of donor atoms in silicon, and charge qubits in QDs.

4. Biexcitons in a Single QD

Piermarocchi *et at.*[33] propose to utilize the robustness of the elementary excitation of the electrons in semiconductor nanostructure QDs, i.e. excitons. An exciton consists of a conduction-band electron and a valence-band hole. This electron–hole pair may be likened to a hydrogen atom, which has an orbiting electron and a nucleus with one proton carrying a positive charge corresponding to the *hole*. In an undoped QD, the optically excited electron–hole pair feels the presence of a large number of atoms (of the order of 10^5–10^6) in the dot and the effect may be well characterized by the static dielectric constant and the electron–hole's effective mass.[37] Thus, the exciton works in the same way as excitations in "giant atoms." A single QD can hold multi-exciton complexes containing many interacting excitons.

Piermarocchi *et al.*[33] consider two electron–hole pairs, each with two confined energy levels, inside a single QD (see Fig. 19). The underlying assumptions for the biexciton model considered in this section according to Ref. 33 are:

(i) The lifetimes of the biexciton and exciton are large enough for the quantum operations involved, and no unintended states will be introduced. Thus, the system evolves in a desirable subspace. This also means that only the optically active states are considered.
(ii) The size of the dot considered is about $40 \times 35 \times 5\,\mathrm{nm}^3$. The electronic levels considered are the first two states derived from the localization of the s-like conduction band states, carrying a spin $\pm\frac{1}{2}$, and the hole levels are derived from the localization of the states in the p-like valence-band heavy hole, carrying a $\pm\frac{3}{2}$ total spin in the direction of the QD growth axis.
(iii) Only the Coulomb interaction between the carriers which conserve their conduction or valence band indices is taken into account. The electron–hole exchange is neglected, whose energy is of the order of μeV and only affects the fine structure of the excitonic levels.

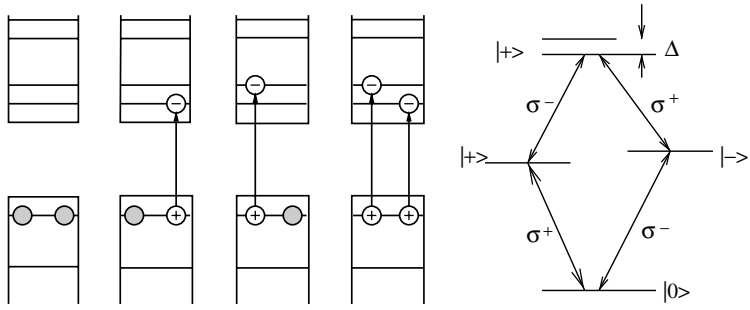

Fig. 19. This schematic illustrating biexciton transitions is adapted from Ref. 25. Here, $\ominus$ represents an electron and $\oplus$ a hole. (a) The four quantum states considered, from left to right: the ground state $|0\rangle$, the excited exciton state $|+\rangle$, the excited exciton state $|-\rangle$ and the biexciton state $|-+\rangle$, which could be utilized to encode $|00\rangle$, $|01\rangle$, $|10\rangle$ and $|11\rangle$, respectively. (b) Diagram of the energy levels of the four states and their transitions induced by optical pulses, where σ^+ represents left-polarized light and σ^- represents right-polarized light. The binding energy is $\Delta = \epsilon_+ + \epsilon_- - \epsilon_{-+}$.

According to the above assumptions, the Hamiltonian of the four-level biexciton system under an optical field with σ^+ polarization can be written as

$$H^+ = \epsilon_+|01\rangle\langle 01| + \epsilon_-|10\rangle\langle 10| + \epsilon_{-+}|11\rangle\langle 11| + \frac{1}{2}\{\Omega_+(t)|01\rangle\langle 00| + f\Omega_+(t)|11\rangle\langle 10| + \text{h.c.}\}, \tag{4.1}$$

where ϵ_+, ϵ_-, and ϵ_{-+} are, respectively, the unperturbed energies of the states $|01\rangle$, $|10\rangle$, and $|11\rangle$ from $|00\rangle$, and h.c. represents the Hermitian conjugate of the operator before it;

$$\Omega_+ = d_+ E_+(t) \tag{4.2}$$

represents a time dependent Rabi energy provided by the electric field, with d_+ being the dipole moment of the exciton state $|+\rangle$; f is a correction factor to the dipole moment due to the Coulomb interaction. The electric field $E_+(t)$ normally has a Gaussian shape: $E_+(t) = \varepsilon_+ e^{-(t/\epsilon)^2} e^{i(\omega_+ t+\phi)}$. If a series of pulses are applied instead of one, $E_+(t)$ is the sum of several pulses and $\Omega_+(t)$ can be expressed as

$$\Omega_+(t) = \sum_j d_+ E_{+,j}(t - \tau_j), \tag{4.3}$$

where τ_j is the center of the jth pulse. The Hamiltonian H^+ may be rewritten in matrix form

$$H^+ = \begin{pmatrix} 0 & \Omega_+^*(t)/2 & 0 & 0 \\ \Omega_+(t)/2 & \epsilon_+ & 0 & 0 \\ 0 & 0 & \epsilon_- & f\Omega_+^*(t)/2 \\ 0 & 0 & f\Omega_+(t)/2 & \epsilon_{-+} \end{pmatrix} \tag{4.4}$$

with respect to the ordered basis $|00\rangle, |01\rangle, |10\rangle, |11\rangle$. The two isolated block forms of the matrix in (4.4) imply that the whole state space can be divided into two invariant subspaces. One is spanned by $|00\rangle$ and $|01\rangle$, or the ground state $|0\rangle$ and excited state $|+\rangle$; the other is spanned by $|10\rangle$ and $|11\rangle$, or the excited sate $|-\rangle$ and biexciton state $|-+\rangle$. The Hamiltonian H^+ introduces Rabi rotation within each subspace, which will be shown in next subsection [cf. (4.15)]. Similarly, the Hamiltonian of the system under σ^- polarized optical field reads

$$\begin{aligned} H^- &= \epsilon_+|01\rangle\langle 01| + \epsilon_-|10\rangle\langle 10| + \epsilon_{-+}|11\rangle\langle 11| \\ &\quad + \frac{1}{2}\{\Omega_-(t)|10\rangle\langle 00| + f\Omega_-(t)|11\rangle\langle 01| + \text{h.c.}\} \end{aligned} \tag{4.5}$$

and the associated matrix form is

$$H^- = \begin{pmatrix} 0 & 0 & \Omega_-^*(t)/2 & 0 \\ 0 & \epsilon_+ & 0 & f\Omega_-^*(t)/2 \\ \Omega_-(t)/2 & 0 & \epsilon_+ & 0 \\ 0 & f\Omega_-(t)/2 & 0 & \epsilon_{-+} \end{pmatrix}. \tag{4.6}$$

We can also write H^- in a similar block matrix form as H^+ in (4.4) by reordering the four basis, while H^- introduces Rabi rotations within subspace spanned by $|00\rangle$ (the ground state $|0\rangle$) and $|10\rangle$ (the excited state $|-\rangle$); and another subspace spanned by $|01\rangle$ (the excited state $|+\rangle$) and $|11\rangle$ ($|-+\rangle$). This is easy to understand because exciton states $|+\rangle$ and $|-\rangle$ are created by optical fields with different polarizations. The fact that H^+ and H^- share the same form after reordering the basis ensures that we only have to focus on one of them. The evolution operator, or propagator, generated by H^- can be obtained easily and similarly after we know the propagator generated by H^+.

4.1. *Derivation of the unitary rotation matrix and the conditional rotation gate*

The key to realizing a logic gate, or unitary transformation, of this quantum system is to choose appropriate optical pulses. Before the derivation of the various logic gates, we first convert H^+ into its interaction picture. We separate H^+ into the unperturbed and interaction parts $H^+ = H_0^+ + H_I^+$, where

$$H_0^+ = \epsilon_+|01\rangle\langle 01| + \epsilon_-|10\rangle\langle 10| + \epsilon_{-+}|11\rangle\langle 11|, \tag{4.7}$$

$$H_I^+ = \frac{1}{2}\{\Omega_+(t)|01\rangle\langle 00| + f\Omega_+(t)|11\rangle\langle 10| + \text{h.c.}\}. \tag{4.8}$$

Standard deduction leads to the Hamiltonian in the interaction picture

$$\begin{aligned} \mathbf{V}^+ &= e^{iH_0^+ t} H_I^+ e^{-iH_0^+ t} \\ &= \frac{1}{2}\{\Omega_+(t)e^{i\epsilon_+ t}|01\rangle\langle 00| + f\Omega_+(t)e^{i(\epsilon_+ - \Delta)t}|11\rangle\langle 10| + \text{h.c.}\}, \end{aligned} \tag{4.9}$$

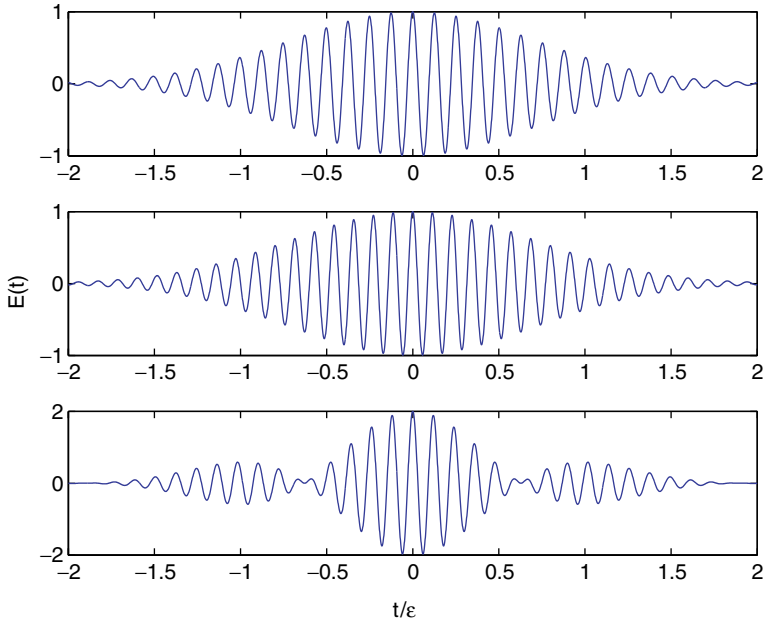

Fig. 20. A schematic illustration of the control pulses applied for a logic gate. The top and middle curves have the same Gaussian shape but different frequencies. The bottom curve is a composite pulse which is the sum of the above two pulses. For simplicity, all the angles are set to 0. Also, $\varepsilon_0 = \varepsilon_1 = 1$ and $\epsilon_0 = \epsilon_1 = \epsilon$. The x-axis represents time; the y-axis represents the amplitude of the electric field.

where $\Delta = \epsilon_+ + \epsilon_- - \epsilon_{-+}$ is the biexciton binding energy, which is not zero because of the interaction between the two excitons. Choosing the optical pulse to be $E_+(t) = \varepsilon_0 e^{-(t/\epsilon_0)^2} e^{-i\epsilon_+ t - i\phi_0} + \varepsilon_1 e^{-(t/\epsilon_1)^2} e^{-i(\epsilon_+ - \Delta)t - i\phi_1}$, a composite bi-chromatic phase-locked pulse shown in Fig. 20, we obtain the Hamiltonian with this pulse, in the interaction picture as

$$\begin{aligned}\mathbf{V}^+ = {} & \frac{d_+}{2}(\varepsilon_0 e^{-(t/\epsilon_0)^2} e^{-i\phi_0} + \varepsilon_1 e^{-(t/\epsilon_1)^2} e^{i\Delta t - i\phi_1})|01\rangle\langle 00| \\ & + \frac{d_+}{2}(\varepsilon_0 e^{-(t/\epsilon_0)^2} e^{-i\Delta t - i\phi_0} + \varepsilon_1 e^{-(t/\epsilon_1)^2} e^{-i\phi_1})|11\rangle\langle 10| + \text{h.c.}, \quad (4.10)\end{aligned}$$

where we have used the usual rotating wave and dipole approximations, and f is set to 1 for convenience. The pulse has an envelope shape $e^{-(t/\epsilon)^2}$ with width 2ϵ, and its spectra has two peaks centered at ϵ_+ and $\epsilon_+ - \Delta$ (see Fig. 20). To determine and approximate the unitary evolution operator, we need the Magnus expansion

$$\begin{aligned}U^+ &= \mathcal{T} e^{-\frac{i}{\hbar}\int_{-\infty}^{\infty} \mathbf{V}^+(t)dt} \\ &= e^{-\frac{i}{\hbar}(\hat{H}^0 + \hat{H}^1 + \cdots)}, \quad (4.11)\end{aligned}$$

where $\mathcal{T}$ is the time ordering operator, and

$$\begin{aligned}\hat{H}^0 &= \int_{-\infty}^{\infty} \mathbf{V}^+(t)dt,\\ \hat{H}^1 &= \int_{-\infty}^{\infty} dt_2 \int_{-\infty}^{\infty} dt_1[\mathbf{V}^+(t_2), \mathbf{V}^+(t_1)],\\ &\vdots \quad \vdots\end{aligned}$$

The two integral limits are set to be infinity, because the amplitude of the electric field decreases to zero exponentially fast. Simulation has shown that the first term already has good accuracy, and the evolution operator can be obtained by the approximation

$$\begin{aligned}U^+ &= e^{-\frac{i}{\hbar}\int_{-\infty}^{\infty} \mathbf{V}^+(t)dt}\\ &= e^{-iA},\end{aligned} \tag{4.12}$$

where

$$\begin{aligned}A &= \frac{1}{\hbar}\int_{-\infty}^{\infty} \mathbf{V}^+(t)dt\\ &= \frac{1}{2}\begin{pmatrix} 0 & e^{i\phi_0}\theta_0 + \delta_1 e^{i\phi_1} & 0 & 0\\ e^{-i\phi_0}\theta_0 + \delta_1 e^{-i\phi_1} & 0 & 0 & 0\\ 0 & 0 & 0 & \delta_0 e^{i\phi_0} + \theta_1 e^{i\phi_1}\\ 0 & 0 & \delta_0 e^{-i\phi_0} + \theta_1 e^{-i\phi_1} & 0\end{pmatrix}\end{aligned} \tag{4.13}$$

in matrix form. Here, for simplicity, we have introduced new variables $\theta_i = \frac{d_+\varepsilon_i}{\hbar} \times \int_{-\infty}^{\infty} e^{-(t/\epsilon_i)^2}dt$ and $\delta_i = \frac{d_+\varepsilon_i}{\hbar}\int_{-\infty}^{\infty} e^{-(t/\epsilon_i)^2}e^{i\Delta t}dt = \frac{\epsilon_i\sqrt{\pi}d_+\varepsilon_i}{\hbar}e^{-(\epsilon\Delta/2)^2}$, $i = 0, 1$. When the pulse is sufficiently flat, $\epsilon\Delta \ll 1$, δ_i is almost zero, and A is further reduced to an even simpler form

$$A = \frac{1}{2}\begin{pmatrix} 0 & e^{i\phi_0}\theta_0 & 0 & 0\\ e^{-i\phi_0}\theta_0 & 0 & 0 & 0\\ 0 & 0 & 0 & e^{i\phi_1}\theta_1\\ 0 & 0 & e^{-i\phi_1}\theta_1 & 0\end{pmatrix}, \tag{4.14}$$

which agrees with the result obtained by the area theorem.[m] It is also worth noting that A is composed of two independent subsystems, which is most convenient in

[m] Assuming θ is the angle the Bloch vector rotates, and $\Omega(t)$ is the Rabi frequency, then the *area theorem* says that

$$\theta = \int_{-\infty}^{t} \Omega(t_1)dt_1,$$

i.e. θ is equal to the area below the frequency curve.

computation. A general form of the propagator U^+ in matrix form can be derived as

$$U^+ = e^{-iA} = \begin{pmatrix} \cos(\theta_0/2) & ie^{i\phi_0}\sin(\theta_0/2) & 0 & 0 \\ ie^{-i\phi_0}\sin(\theta_0/2) & \cos(\theta_0/2) & 0 & 0 \\ 0 & 0 & \cos(\theta_1/2) & ie^{i\phi_1}\sin(\theta_1/2) \\ 0 & 0 & ie^{-i\phi_1}\sin(\theta_1/2) & \cos(\theta_1/2) \end{pmatrix}. \tag{4.15}$$

The matrix in (4.15) is useful in the design of pulses for the 1-bit rotations and the conditional rotation gates.

Theorem 5. *In the above four-level biexciton quantum system* (*within the accuracy of the area theorem*), *polarized optical pulses can be used to realize unitary* 1*-bit rotation and the conditional rotation matrices.*

Proof. When $\theta_0 = \theta_1 = \theta$, from (4.15), we obtain the y-rotation of the first qubit by setting $\phi_0 = \phi_1 = \pi/2$, denoted by $R_{1y}(\theta)$, and the x-rotation $R_{1x}(\theta)$ by setting $\phi_0 = \phi_1 = 0$. If $\theta_0 = 0$, a rotation of first qubit when the second qubit is in state $|1\rangle$ is obtained, denoted by $C_{1,2}^{\mathrm{ROT}}(\theta, \phi)$:

$$C_{1,2}^{\mathrm{ROT}}(\theta, \phi) = \begin{pmatrix} 1 & 0 & 0 & 0 \\ 0 & 1 & 0 & 0 \\ 0 & 0 & \cos(\theta/2) & ie^{i\phi}\sin(\theta/2) \\ 0 & 0 & ie^{-i\phi}\sin(\theta/2) & \cos(\theta/2) \end{pmatrix}. \tag{4.16}$$

Another conditional rotation triggered when the second qubit is in state $|0\rangle$ can be obtained with $\theta_1 = 0$, denoted by $C_{1,\bar{2}}^{\mathrm{ROT}}(\theta, \phi)$:

$$C_{1,\bar{2}}^{\mathrm{ROT}}(\theta, \phi) = \begin{pmatrix} \cos(\theta/2) & ie^{i\phi}\sin(\theta/2) & 0 & 0 \\ ie^{-i\phi}\sin(\theta/2) & \cos(\theta/2) & 0 & 0 \\ 0 & 0 & 1 & 0 \\ 0 & 0 & 0 & 1 \end{pmatrix}. \tag{4.17}$$

The proof of the rotations and conditional rotations of the second qubit is similar. We only need to apply the σ^- polarized field instead of the σ^+ polarized field. The result can be obtain by just reordering the basis.

The derivation of the above theorem also provides blocks to construct a CNOT gate, and we have the following corollary.

Corollary 3. *A CNOT gate can be simulated with the one qubit rotation and conditional rotation gates obtained in the above theorem*; *thus, the proposal is universal.*

Proof. We will only investigate the CNOT gate controlled by the second qubit. Using the same notation as in the last theorem, we can construct a z-rotation operation of the second qubit:

$$R_{2z}(\theta) = R_{2y}(\pi/2)R_{2x}(\theta)R_{2y}(-\pi/2) \tag{4.18}$$

and a special case,

$$\begin{aligned} R_{2z}(\pi/2) &= R_{2y}(\pi/2)R_{2x}(\pi/2)R_{2y}(-\pi/2) \\ &= \begin{pmatrix} e^{-\pi/4} & 0 & 0 & 0 \\ 0 & e^{-\pi/4} & 0 & 0 \\ 0 & 0 & e^{\pi/4} & 0 \\ 0 & 0 & 0 & e^{\pi/4} \end{pmatrix}. \end{aligned} \tag{4.19}$$

The above z-rotation can be used in a quantum phase gate Q_π up to a phase shift:

$$\begin{aligned} Q_\pi &= R_{2z}(\pi/2)R_{1y}(\pi/2)R_{1x}(\pi/2)C_{1,2}^{\mathrm{ROT}}(-\pi/2)C_{1,2}^{\mathrm{ROT}}(\pi/2)R_{1y}(-\pi/2) \\ &= e^{-i\pi/4}\begin{pmatrix} 1 & 0 & 0 & 0 \\ 0 & 1 & 0 & 0 \\ 0 & 0 & 1 & 0 \\ 0 & 0 & 0 & -1 \end{pmatrix}. \end{aligned} \tag{4.20}$$

Now we can construct the CNOT gate with the second qubit as the control qubit using above phase shift gate and a conditional rotational gate combined as

$$\begin{aligned} C_{1,2}^{\mathrm{NOT}} &= Q_\pi C_{1,2}^{\mathrm{ROT}}(\pi, -\pi/2) \\ &= e^{-i\pi/2}\begin{pmatrix} 1 & 0 & 0 & 0 \\ 0 & 1 & 0 & 0 \\ 0 & 0 & 0 & 1 \\ 0 & 0 & 1 & 0 \end{pmatrix}, \end{aligned} \tag{4.21}$$

up to a phase factor.

4.2. *Decoherence and measurement*

The lifetime of an exciton is critical to quantum information processing. It constrains how many logical operations can be performed before the system loses coherence. Theoretical and experimental results[5,40] show that the lifetime spans from 10 ps to about 1 ns, depending on the confinement and temperature. The source of decoherence comes from spontaneous emission caused by ambient fluctuations and other factors. The shape of the pulse should be carefully designed to reduce the spillover of unwanted excited states, such as unlocalized exciton states with energy levels close to that of the localized excitons. During the operations, the heating effect may also accelerate the decoherence.

Research on coherent nonlinear optical spectroscopy of the individual excitons provides a method to probe a single exciton in a semiconductor QD.[6,40] When a

weak probe optical pulse $E(t)$ is applied on the QD, an induced nonlinear optical polarization field is created. The polarization field is homodyne detected with the transmitted field, generating a signal. The integral of this signal provides a differential transmission signal proportional to the inversion of the exciton, i.e. the difference of probability amplitudes of the excited and ground states.

4.3. *Proposals for coupling of two or more biexciton QD*

It is not realistic to set up more qubits by exciting more excitons in a single QD. To make the above proposal *scalable*, other strategies to couple two or more QDs are necessary. Potential candidates include a microcavity[36] as already discussed in Sec. 2, where the cavity mode photon is used as an agent to connect two QD, and a linear support,[7] where the quantum phonon state of a big molecule or nanorod serves as the data bus. Piermarocchi *et al.*[34] also suggest using pure optical control to couple spins in two neighboring QD. The main control method is to use an external optical field with σ^+ polarization which creates an unlocalized electron–hole pair, i.e. an exciton. This photo-generated electron–hole pair has a fixed angular momentum configuration corresponding to the polarization of the field, with electron spin state $-\sigma(-1/2)$ and hole spin state $\sigma(3/2)$. The density of the optical field is kept below the lowest discrete exciton state. The electron spin in the photo-generated exciton interacts with the two electron spins from the two neighboring QDs and serves as an agent to couple them together. After reasonable simplification, the interaction Hamiltonian between the two spins can be shown to be

$$H_S = -2J_{12}\boldsymbol{S}^1 \cdot \boldsymbol{S}^2, \tag{4.22}$$

where $\boldsymbol{S}^1$ and $\boldsymbol{S}^2$ are the two electron spins from the two QDs, and J_{12} is a constant. Figure 21 gives a schematic of this proposal. It is an interaction term similar to that of NMR except that the constant J_{12} is controllable.

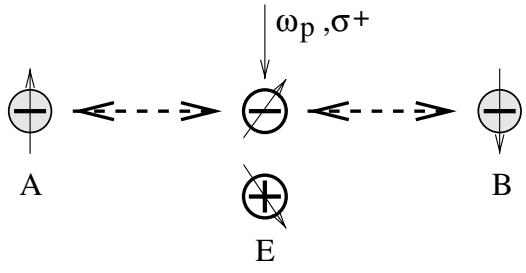

Fig. 21. A schematic of the optical induced spin–spin interaction. A and B are two electron spins in two neighboring quantum dots; E is the photo-generated unlocalized exciton which interacts with A and B. The optical field has frequency ω_p and σ^+ polarization.

5. Conclusions

Physical implementations of qubits using QDs are fundamentally limited by interaction of qubits with their environment and the resulting decoherence. These interactions of the qubits set the maximum time of coherent operation and an upper bound for the number of quantum gate operations to be applied on a single qubit; therefore, understanding the origin of decoherence is critical in controlling or reducing it, in order to implement quantum logic gates. Because of their strong localization in all directions, electrons confined in QDs are strongly coupled to longitudinal optical (LO) vibrations of the underlying crystal lattice. If the coupling strength exceeds the "continuum width," the energy of keeping the LO phonons delocalized, a continuous Rabi oscillation of the electron arises, that is, an everlasting emission and absorption of one LO phonon. As a result, electron–phonon entangled quasi-particles known as polarons form; these play a substantial role in the rapid decoherence of the spin-based QD qubits. The decoherence time for an exciton typically ranges from 20 ps to 100 ps, which is considerably shorter than the decoherence times of nuclear or electron spin. This is a problem since gate operations take approximately 40 ps to perform. However, implementing ultrafast (femtosecond) optoelectronics may eventually enable us to bypass this problem. Read-out on the QD can be achieved by placing the excitation and probe beam spots at a specific location where a number of qubits with different excitonic frequencies can be accessed. The somewhat randomized distribution of the QD size and composition allow qubits with different excitation frequencies to exist, making it easier to identify specific qubits by singling out the different frequencies.

There are many interesting or useful websites on QDs or quantum complexity in general, maintained by individual researchers or research centers. We mention just a few of them here:

(i) Reference 49, of the Centre for Quantum Computation, at Oxford University, UK, contains comprehensive, current information and activities in quantum computation.
(ii) Reference 50, of the Los Alamos National Laboratory, US, contains perhaps the most current papers and manuscripts on any quantum-related topics.
(iii) Reference 51, Quantum Dot Group homepage, maintained by a group of European (mainly French) researchers.
(iv) Reference 52, maintained by researchers in Oxford and Cambridge Universities, UK, on optical quantum dots.
(v) Reference 53, maintained by L. Kouwenhoven of the Technical University of Delft in the Netherlands.
(vi) Reference 54, maintained by researchers in the Electrical Engineering Department of the University of Notre Dame, US, is the website of quantum cellular automata.

Acknowledgement

We thank the referee for helpful comments and constructive criticism, which have improved the paper. G. Chen is supported in part by a DARPA QuIST grant, and by a TITF grant from Texas A&M University. A. Neogi is supported in part by a Faculty Research Grant from the University of North Texas. Z. Diao is supported in part by a Research Challenge Award and an OURC Award from Ohio University, USA. The authors thank Prof. Kawazoe at the University of Tokyo, Japan for the measurement of near-field optical spectroscopy and Prof. Hadis Morkoc at Virginia Commonwealth University, USA for the synthesis of GaN quantum dots.

Appendix A. The Fock–Darwin States

The mathematical derivations of (3.4) rely heavily on the Fock–Darwin Hamiltonian, which models the motion of a conduction-band electron confined in a two-dimensional parabolic potential well in an external magnetic field perpendicular to the two-dimensional plane:

$$H_{\mathrm{FD}} = \frac{1}{2m}\left|\boldsymbol{p} - \frac{e}{c}\boldsymbol{A}\right|^2 + \frac{1}{2M}\omega_0^2 r^2 \quad (r = (x^2+y^2)^{1/2}), \tag{A.1}$$

where the notation follows that introduced in Sec. 3.3. The Fock–Darwin Hamiltonian H_{FD} and its eigenstates have pleasant mathematical properties[12,15] and may be viewed as a two-dimensional analog of the simple harmonic oscillator.

From (A.1) and (3.5), we have

$$\begin{aligned} H &= \frac{1}{2m}\left(|\boldsymbol{p}|^2 - 2\frac{e}{c}\boldsymbol{p}\cdot\boldsymbol{A} + \frac{e^2}{c^2}|\boldsymbol{A}|^2\right) + \frac{1}{2}m\omega_0^2(x^2+y^2) \\ &= \frac{|\boldsymbol{p}|^2}{2m} - \frac{1}{2}\frac{eB}{mc}(-p_x y + p_y x) + \frac{e^2B^2}{8mc^2}(x^2+y^2) + \frac{1}{2}m\omega_0^2(x^2+y^2) \\ &= \frac{|\boldsymbol{p}|^2}{2m} + \frac{1}{2}m\left(\omega_0^2 + \frac{\omega_c^2}{4}\right)(x^2+y^2) + \frac{1}{2}\omega_c L_z, \end{aligned} \tag{A.2}$$

where

$\frac{eB}{mc} \equiv \omega_c =$ the cyclotron frequency,
$L_z = xp_y - yp_x =$ the z-component of the angular momentum, $\boldsymbol{L} = \boldsymbol{r}\times\boldsymbol{p}$.

Next, from the four independent operators x, y, p_x and p_y, we define four new operators:

$$\left.\begin{aligned} a &= \varepsilon(x - iy) + \eta(ip_x + p_y), \\ a^+ &= \varepsilon(x + iy) + \eta(-ip_x + p_y), \\ b &= \varepsilon(x + iy) + \eta(ip_x - p_y), \\ b^+ &= \varepsilon(x - iy) + \eta(-ip_x - p_y), \end{aligned}\right\} \tag{A.3}$$

where ε and η are real numbers. Using (Poisson brackets)

$$[x, p_x] = [y, p_y] = i\hbar, \tag{A.4}$$

$$[x, y] = [x, p_y] = [y, x] = [y, p_x] = 0, \tag{A.5}$$

we can easily show that

$$[a^+, b] = [a, b^+] = [a, b] = [a^+, b^+] = 0, \tag{A.6}$$

and

$$\begin{aligned}[a^+, a] &= \varepsilon\eta[x + iy, ip_x + p_y] + \varepsilon\eta[-ip_x + p_y, x - iy] \\ &= -4\varepsilon\eta\hbar, \end{aligned} \tag{A.7}$$

$$\begin{aligned}[b^+, b] &= \varepsilon\eta[x - iy, ip_x - p_y] + [-ip_x - p_y, x + iy] \\ &= -4\varepsilon\eta\hbar. \end{aligned} \tag{A.8}$$

Thus, if we choose

$$\eta = 1/(4\varepsilon\hbar), \tag{A.9}$$

then

$$\begin{cases} [a, a^+] = [b, b^+] = 1; \\ \text{all other commutators are zero.} \end{cases} \tag{A.10}$$

We obtain

$$\begin{aligned} p_x^2 + p_y^2 &= (ip_x + p_y)(-ip_x + p_y) \\ &= \left(\frac{a - b^+}{2\eta}\right)\left(\frac{a^+ - b}{2\eta}\right), \end{aligned} \tag{A.11}$$

$$\begin{aligned} x^2 + y^2 &= (x + iy)(x - iy) \\ &= \left(\frac{a^+ + b}{2\varepsilon}\right)\left(\frac{a + b^+}{2\varepsilon}\right), \end{aligned} \tag{A.12}$$

and

$$\begin{aligned} L_z = xp_y - yp_x &= \frac{1}{2}[(x + iy)(ip_x + p_y) - (x - iy)(ip_x - ip_y)] \\ &= \frac{1}{2}\left[\left(\frac{a^+ + b}{2\varepsilon}\right)\left(\frac{a - b^+}{2\eta}\right) - \left(\frac{a + b^+}{2\varepsilon}\right)\left(\frac{b - a^+}{2\eta}\right)\right]. \end{aligned} \tag{A.13}$$

Define

$$\Omega^2 = \omega_0^2 + \frac{\omega_c^2}{4}. \tag{A.14}$$

Then

$$\begin{aligned}H &= \frac{1}{2m}\frac{1}{4\eta^2}(a-b^+)(a^+-b)+\frac{1}{2}m\Omega^2\cdot\frac{1}{4\varepsilon^2}(a^++b)(a+b^+)\\ &\quad+\frac{1}{2}\omega_c\cdot\frac{1}{8\varepsilon\eta}[(a^++b)(a-b^-)-(a+b^+)(b-a^+)]\\ &= \frac{1}{8m\eta^2}(aa^+-ab-b^+a^++b^+b)+\frac{m\Omega^2}{8\varepsilon^2}(a^+a+a^+b^++ba+bb^+)\\ &\quad+\frac{\omega_c}{16\varepsilon\eta}(a^+a+b\not{a}-a^+\not{b}^+-bb^+-a\not{b}+aa^+-b^+b+b^+\not{a}^+).\end{aligned} \tag{A.15}$$

Recall from (A.9) that $1/\eta = 4\varepsilon\hbar$. If we further require that

$$\frac{1}{8m\eta^2} = \frac{m\Omega^2}{8\varepsilon^2} = \frac{m\Omega^2}{8}(4\eta\hbar)^2 = 2m\Omega^2\eta^2\hbar^2,$$

i.e.

$$\eta = \frac{1}{2\sqrt{\hbar m\Omega}}, \tag{A.16}$$

then from (A.15), we see that cross-terms ab, ab^+, a^+b, a^+b^+, etc. cancel out:

$$\begin{aligned}H &= \frac{\hbar\Omega}{2}\{[aa^+-a\not{b}-b^+\not{a}^++b^+b]+[a^+a+a^+\not{b}^++b\not{a}+bb^+]\}\\ &\quad+\frac{\hbar\omega_c}{4}[\underbrace{a^+a+aa^+}_{2a^+a+\mathbf{1}}\underbrace{-bb^+-b^+b}_{-2b^+b-\mathbf{1}}]\\ &= \frac{\hbar\Omega}{2}[2a^+a+\mathbf{1}+2b^+b+\mathbf{1}]+\frac{\hbar\omega_c}{2}[a^+a-b^+b]\\ &= \hbar\left(\Omega+\frac{\omega_c}{2}\right)\left(a^+a+\frac{1}{2}\right)+\hbar\left(\Omega-\frac{\omega_c}{2}\right)\left(b^+b+\frac{1}{2}\right)\\ &= \hbar\omega_+\left[a^+a+\frac{1}{2}\right]+\hbar\omega_-\left[b^+b+\frac{1}{2}\right],\end{aligned} \tag{A.17}$$

where

$$\omega_\pm \equiv \Omega \pm \frac{\omega_c}{2}. \tag{A.18}$$

We can now define the Fock–Darwin states

$$|n_+,n_-\rangle = \frac{1}{[(n_+!)(n_-!)]^{1/2}}(a^+)^{n_+}(b^+)^{n_-}|0,0\rangle, \tag{A.19}$$

for any integers n_+ and n_-, $n_+\geq 0$, $n_-\geq 0$, where

$$\begin{cases}a = \varepsilon(x-iy)+\eta(ip_x+p_y),\\ b = \varepsilon(x+iy)+\eta(ip_x-p_y),\end{cases} \tag{A.20}$$

with

$$\eta = \frac{1}{2\sqrt{\hbar m\Omega}}, \qquad \varepsilon = \frac{1}{4\hbar\eta} = \frac{1}{4\hbar}\cdot 2\sqrt{\hbar m\Omega} = \frac{1}{2}\sqrt{\frac{m\Omega}{\hbar}}. \tag{A.21}$$

From (A.17)–(A.19), we have

$$H|n_+, n_-\rangle = \left[\hbar\omega_+ \left(n_+ + \frac{1}{2}\right) + \hbar\omega_- \left(n_- + \frac{1}{2}\right)\right] |n_+, n_-\rangle, \tag{A.22}$$

for integers $n_+ \geq 0, n_- \geq 0$.

Instead of using x and y, we can also use the complex variable z and its conjugate $\bar{z}$:

$$z = x + iy, \quad \bar{z} = x - iy. \tag{A.23}$$

Then

$$\begin{cases} \partial_x = \dfrac{\partial}{\partial x} = \dfrac{\partial z}{\partial x}\dfrac{\partial}{\partial z} + \dfrac{\partial \bar{z}}{\partial x}\dfrac{\partial}{\partial \bar{z}} = \partial_z + \bar{\partial}_z, \\ \partial_y = \dfrac{\partial}{\partial y} = \dfrac{\partial z}{\partial y}\dfrac{\partial}{\partial z} + \dfrac{\partial \bar{z}}{\partial y}\dfrac{\partial}{\partial \bar{z}} = i\partial_z - i\bar{\partial}_z, \end{cases} \tag{A.24}$$

from where we obtain in turn

$$\partial_z = \frac{1}{2}(\partial_x - i\partial_y), \quad \bar{\partial}_z = \frac{1}{2}(\partial_x + i\partial_y). \tag{A.25}$$

From (A.19)–(A.25), we thus have

$$\begin{cases} a = \dfrac{1}{2}\sqrt{\dfrac{m\Omega}{\hbar}}\ \bar{z} + \dfrac{1}{2\sqrt{\hbar m\Omega}} 2\hbar\partial_z = \dfrac{1}{\sqrt{2}}\left[\dfrac{\bar{z}}{2\ell_0} + 2\ell_0\partial_z\right], \\ b = \dfrac{1}{2}\sqrt{\dfrac{m\Omega}{\hbar}}\ z + \dfrac{1}{2\sqrt{\hbar m\Omega}} 2\hbar\bar{\partial}_z = \dfrac{1}{\sqrt{2}}\left[\dfrac{z}{2\ell_0} + 2\ell_0\bar{\partial}_z\right], \end{cases} \tag{A.26}$$

where $\ell_0 \equiv [\hbar/(2m\Omega)]^{1/2}$.

Theorem A.1. *The ground state of the Fock–Darwin states are given by*

$$|0, 0\rangle = \sqrt{\frac{m\Omega}{\pi\hbar}} e^{-\frac{m\Omega}{2\hbar}(x^2+y^2)}. \tag{A.27}$$

Proof. Since

$$a|0, 0\rangle = 0,$$

we have

$$|0, 0\rangle = \tilde{c}e^{-\frac{m\Omega}{2\hbar}\bar{z}z}, \tag{A.28}$$

where c is a normalization constant. We also see that (A.28) satisfies

$$b|0, 0\rangle = 0.$$

Thus

$$|0, 0\rangle = \tilde{c}e^{-\frac{m\Omega}{2\hbar}(x^2+y^2)}.$$

The constant of normalization is easily computed to be $\tilde{c} = [(m\Omega)/(\pi\hbar)]^{1/2}$. The rest can also be easily verified.

Appendix B Evaluation of the Exchange Energy

The point of view taken by Burkard, Loss and DiVincenzo[10] is to regard the two coupled QDs as a "molecule" obtained by combining two QDs through perturbation with a Fock–Darwin-like ground state as the ground state of the single electron spin on each dot.

Let us rewrite the overall Hamiltonian in (3.10) of the coupled system as

$$H_{\rm orb} = H_1(\boldsymbol{p}_1, \boldsymbol{r}_1) + H_2(\boldsymbol{p}_2, \boldsymbol{r}_2) + C(\boldsymbol{r}_1, \boldsymbol{r}_2) + W(\boldsymbol{r}_1, \boldsymbol{r}_2), \tag{B.1}$$

$$(\boldsymbol{p}_1 = (p_{x_1}, p_{y_1}, 0),\ \boldsymbol{r}_1 = (x_1, y_1),\ \boldsymbol{p}_2 = (p_{x_2}, p_{y_2}, 0),\ \boldsymbol{r}_2 = (x_2, y_2))$$

$$H_1(\boldsymbol{p}_1, \boldsymbol{r}_1) = \frac{1}{2m}\Big|\boldsymbol{p}_1 - \frac{e}{c}\boldsymbol{A}(x_1, y_1, 0)\Big|^2 + eEx_1 + \frac{m\omega_0^2}{2}[(x_1 + a)^2 + y_1^2], \tag{B.2}$$

$$H_2(\boldsymbol{p}_2, \boldsymbol{r}_2) = \frac{1}{2m}\Big|\boldsymbol{p}_2 - \frac{e}{c}\boldsymbol{A}(x_2, y_2, 0)\Big|^2 + eEx_2 + \frac{m\omega_0^2}{2}[(x_2 - a)^2 + y_2^2], \tag{B.3}$$

$$C(\boldsymbol{r}_1, \boldsymbol{r}_2) = \frac{e^2}{\kappa|\boldsymbol{r}_1 - \boldsymbol{r}_2|} \quad \text{[the same as (3.8)]},$$

$$W(\boldsymbol{r}_1, \boldsymbol{r}_2) = W_1(x_1) + W_2(x_2), \tag{B.4}$$

with

$$W_j(x_j) \equiv \frac{m\omega_0^2}{2}\left[\frac{1}{4a^2}(x_j^2 - a^2)^2 - (x_j - a)^2\right], \text{ for } j = 1, 2. \tag{B.5}$$

H_1 and H_2 given above are not Fock–Darwin Hamiltonians. However, after simple similarity transformations, they become Fock–Darwin plus a constant.

Lemma B.1. *Given H_1 and H_2 as in (B.1) and (B.3), define*

$$\left.\begin{aligned}\widetilde{H}_1 &= e^{\frac{i}{\hbar}\left(\frac{e^2BE}{2m\omega_0^2c} + \frac{eBa}{2c}\right)y_1} H_1 e^{-\frac{i}{\hbar}\left(\frac{e^2BE}{2m\omega_0^2c} + \frac{eBa}{2c}\right)y_1},\\ \widetilde{H}_2 &= e^{\frac{i}{\hbar}\left(\frac{e^2BE}{2m\omega_0^2c} - \frac{eBa}{2c}\right)y_2} H_2 e^{-\frac{i}{\hbar}\left(\frac{e^2BE}{2m\omega_0^2c} - \frac{eBa}{2c}\right)y_2}.\end{aligned}\right\} \tag{B.6}$$

Then

$$\widetilde{H}_j = H_{j,\rm FD} - \left(-\frac{e^2E^2}{2m\omega_0^2} \mp eEa\right); \quad \text{"}-\text{"} \textit{ for } j = 1, \text{ "}+\text{"} \textit{ for } j = 2, \tag{B.7}$$

where $H_{j,\rm FD}$ is a Fock–Darwin Hamiltonian for $j = 1, 2$ defined by

$$H_{j,\rm FD} = \frac{1}{2m}\left|\boldsymbol{p}_j - \frac{e}{c}\boldsymbol{A}(x_{j\mp}, y_j, 0)\right|^2 + \frac{m\omega_0^2}{2}(x_{j\mp}^2 + y_j^2); \tag{B.8}$$

where

$$x_{j\mp} \equiv x_j - (-1)^j a + \frac{eE}{m\omega_0^2}, \tag{B.9}$$

and "$-$" for $j = 1$ and "$+$" for $j = 2$.

Proof. For $j = 1$, the similarity transformation $(\text{B.6})_1$ effects a translation of p_{y_1}, the y-component of $\boldsymbol{p}_1$, as follows

$$p_{y_1} \to p_{y_1} + \frac{e^2BE}{2m\omega_0^2 c} + \frac{eBa}{2c}, \tag{B.10}$$

while the remaining variables x_1, y_1 and p_{x_1} are left unchanged. Thus, from (B.6)

$$\widetilde{H}_1 = \frac{1}{2m}\left[\left(p_{x_1} + \frac{eBy_1}{2c}\right)^2 + \left(p_{y_1} - \frac{e^2BE}{2m\omega_0^2 c} + \frac{eBa}{2c} - \frac{eBx_1}{2c}\right)^2\right]$$
$$+ \frac{m\omega_0^2}{2}\left[\left(x_1 - a + \frac{eE}{m\omega_0^2}\right)^2 + y_1^2\right] - eE\left(\frac{eE}{2m\omega_0^2} - a\right). \tag{B.11}$$

Define

$$x_1 = x_1 + a + \frac{eE}{m\omega_0^2} \tag{B.12}$$

as in (B.9). Then

$$\widetilde{H}_1 = \frac{1}{2m}\left|\overrightarrow{p}_1 - \frac{e}{c}\overrightarrow{A}\,(x_{1-}, y_1, 0)\right|^2 + \frac{m\omega_0^2}{2}(x_{1-}^2 + y_1^2) - \frac{e^2E^2}{2m\omega_0^2} + eEa \tag{B.13}$$

$$\equiv H_{1,\hat{\text{FD}}} + \left(eEa - \frac{e^2E^2}{2m\omega_0^2}\right), \tag{B.14}$$

where $H_{1,\text{FD}}$ is a Fock–Darwin Hamiltonian (of variables $\boldsymbol{p}_1, x_{1-}$ and y_1). H_2 and $\widetilde{H}_2$ can be similarly treated.

We thus have

$$H_1 = e^{-\frac{i}{\hbar}\left(\frac{e^2BE}{2m\omega_0^2 c} - \frac{eBa}{2c}\right)y_1} H_{1,\text{FD}} e^{\frac{i}{\hbar}\left(\frac{e^2BE}{2m\omega_0^2 c} - \frac{eBa}{2c}\right)y_1} + \left(eEa - \frac{e^2E^2}{2m\omega_0^2}\right), \tag{B.15}$$

whose eigenstates are

$$e^{-\frac{i}{\hbar}\left(\frac{e^2BE}{2m\omega_0^2 c} - \frac{eBa}{2c}\right)y_1}|n_+^{(1)}, n_-^{(1)}\rangle \quad [\text{cf. (A.22)}], \tag{B.16}$$

with eigenvalues

$$\varepsilon(n_+^{(1)} n_-^{(1)}) \equiv \hbar\omega_+\left(n_+^{(1)} + \frac{1}{2}\right) + \hbar\omega_-\left(n_-^{(1)} + \frac{1}{2}\right) + \left(eEa - \frac{eE^2}{2m\omega_0^2}\right), \tag{B.17}$$

$$\left(\omega_\omega \equiv \sqrt{\omega_0^2 + \left(\frac{eB}{2mc}\right)^2} \pm \frac{eB}{2mc}\right). \tag{B.18}$$

Similarly, H_2 and $H_{2,\text{FD}}$ can be obtained from (B.3), (B.14) and (B.15) by simply replacing the index 1 by 2 and x_- by

$$x_+ \equiv x - a + \frac{eE}{m\omega_0^2}. \tag{B.19}$$

Since the ground state $|0,0\rangle$ of the Fock–Darwin Hamiltonian, $H_{\rm FD}$, is [cf. (A.27)]

$$\Phi_0(x,y)=\sqrt{\frac{m\Omega}{\pi\hbar}}e^{-\frac{m\Omega}{2\hbar}(x^2+y^2)} \qquad \left(\Omega\equiv\sqrt{\omega_0^2+\left(\frac{eB}{2mc}\right)^2}\right),$$

therefore, the ground state of the Hamiltonians H_1 and H_2 are, respectively,

$$\Phi_0^{(1)}(x,y)=e^{-\frac{i}{\hbar}\left(\frac{e^2B_E}{2m\omega_0^2c}+\frac{eBa}{2c}\right)y}\sqrt{\frac{m\Omega}{\pi\hbar}}e^{-\frac{m\Omega}{2\hbar}(x_-^2+y^2)}, \tag{B.20}$$

$$\Phi_0^{(2)}(x,y)=e^{-\frac{i}{\hbar}\left(\frac{e^2B_E}{2m\omega_0^2c}-\frac{eBa}{2c}\right)y}\sqrt{\frac{m\Omega}{\pi\hbar}}e^{-\frac{m\Omega}{2\hbar}(x_+^2+y^2)}. \tag{B.21}$$

We are now in a position to apply the well-known Heitler–London method in quantum molecular chemistry to model the coupled system. The method utilizes "quantum dot" orbitals:

$$\left.\begin{aligned} a(j)&\equiv\Phi_0^{(1)}(x_j,y_j), \quad j=1,2,\\ b(j)&\equiv\Phi_0^{(2)}(x_j,y_j), \quad j=1,2,\end{aligned}\right\} \tag{B.22}$$

from which we further define

$$|\Psi_\pm\rangle=\nu[a(1)b(2)\pm a(2)b(1)], \tag{B.23}$$

where ν is the normalization factor. Note that $|\Psi_+\rangle$ is the singlet state, while $|\Psi_-\rangle$ is the triplet state. Note that our notation in (B.21) and (B.23) follows from the convention used by Slater (Ref. 10, Chap. 3).

Lemma B.2. *We have the overlap integral*

$$S\equiv\langle\Phi_0^{(2)}|\Phi_0^{(1)}\rangle=e^{-bd^2-d^2(b-\frac{1}{b})}, \tag{B.24}$$

where

$$b\equiv\frac{\Omega}{\omega_0}, \quad d=(m\omega_0/\hbar)^{1/2}a. \tag{B.25}$$

Consequently, the normalized singlet and triplet states are

$$|\Psi_\pm\rangle=\frac{1}{\sqrt{2(1\pm S^2)}}[a(1)b(2)\pm a(2)b(1)], \tag{B.26}$$

satisfying

$$\langle\Psi_+|\Psi_+\rangle=1, \quad \langle\Psi_-|\Psi_-\rangle=1$$

and

$$\langle\Psi_+|\Psi_-\rangle=0.$$

Proof. We evaluate (B.24):

$$
\begin{aligned}
S &\equiv \int_{-\infty}^{\infty}\int_{-\infty}^{\infty} \bar{\Phi}_0^{(2)}(x,y)\Phi_0^{(1)}(x,y)dxdy \\
&= \int_{-\infty}^{\infty}\int_{-\infty}^{\infty} e^{-\frac{i}{\hbar}\left(\frac{e^2BE}{2m\omega_0^2c}+\frac{eBa}{2C}-\frac{e^2BE}{2m\omega_0^2c}+\frac{eBa}{2c}\right)y}\cdot\frac{m\Omega}{\pi\hbar}\cdot e^{-\frac{m\Omega}{\hbar}\left[\left(x+\frac{eE}{m\omega_0^2}\right)^2+a^2+y^2\right]}dxdy \\
&= e^{-\frac{m\Omega}{\hbar}a^2-\frac{e^2B^2a^2}{4\hbar m\Omega c^2}}\left(\frac{m\Omega}{\pi\hbar}\right)\underbrace{\int_{-\infty}^{\infty} e^{-\frac{m\Omega}{\hbar}\left(x+\frac{eE}{m\omega_0^2}\right)^2}dx}_{\sqrt{\frac{\pi}{(m\Omega/\hbar)}}}\cdot\underbrace{\int_{-\infty}^{\infty} e^{-\frac{m\Omega}{\hbar}\left(y+i\frac{eBa}{2m\Omega c}\right)^2}dy}_{\sqrt{\frac{\pi}{(m\Omega/\hbar)}}} \\
&= e^{-\frac{m\Omega}{\hbar}a^2-\frac{e^2B^2a^2}{4\hbar m\Omega c^2}} = e^{-bd^2-d^2(b-\frac{1}{2})}.
\end{aligned}
$$

The rest follows from straightforward calculations.

The exchange energy, from (3.12), can now be written as

$$
\begin{aligned}
J &\equiv \langle\Psi_-|H_{\rm orb}|\Psi_-\rangle - \langle\Psi_+|H_{\rm orb}|\Psi_+\rangle \\
&= \frac{1}{2(1-S^2)}\big\{\langle a(1)b(2)|H_{\rm orb}|a(1)b(2)\rangle + \langle a(2)b(1)|H_{\rm orb}|a(2)b(1)\rangle \\
&\quad - \langle a(1)b(2)|H_{\rm orb}|a(2)b(1)\rangle - \langle a(2)b(1)|H_{\rm orb}|a(1)b(2)\rangle\big\} \\
&\quad - \frac{1}{2(1+S^2)}\big\{\langle a(1)b(2)|H_{\rm orb}|a(1)b(2)\rangle + \langle a(2)b(1)|H_{\rm orb}|a(2)b(1)\rangle \\
&\quad + \langle a(1)b(2)|H_{\rm orb}|a(2)b(1)\rangle + \langle a(2)b(1)|H_{\rm orb}|a(1)b(2)\rangle\big\} \\
&= \cdots (\text{combining the two parentheses, using (B.1) and expanding}) \\
&= \frac{S^2}{1-S^4}\big\{\big[\langle a(1)|H_1|a(1)\rangle + \langle a(2)|H_2|a(2)\rangle + \langle b(1)|H_1|b(1)\rangle + \langle a(2)|H_2|a(2)\rangle\big] \\
&\quad - \frac{1}{S^2}\big[\langle a(1)|H_1|b(1)\rangle\langle b(2)|a(2)\rangle + \langle b(2)|H_2|a(2)\rangle\langle a(1)|b(1)\rangle \\
&\quad + \langle b(1)|H_1|a(1)\rangle\langle a(2)|b(2)\rangle + \langle a(2)|H_2|b(2)\rangle\langle b(1)|a(1)\rangle\big] \\
&\quad + \big[\langle a(1)b(2)|C|a(1)b(2)\rangle + \langle a(2)b(1)|C|a(2)b(1)\rangle\big] \\
&\quad - \frac{1}{S^2}\big[\langle a(1)b(2)|C|a(2)b(1)\rangle + \langle a(2)b(1)|C|a(1)b(2)\rangle\big] \\
&\quad + \big[\langle a(1)b(2)|W|a(1)b(2)\rangle + \langle a(2)b(1)|W|a(2)b(1)\rangle \\
&\quad - \frac{1}{S^2}\big(\langle a(1)b(2)|W|a(2)b(1)\rangle + \langle a(2)b(1)|W|a(1)b(2)\rangle\big)\big]\big\} \qquad \text{(B.27)} \\
&\equiv \frac{S^2}{1-S^4}\left\{\mathfrak{B}_1 - \frac{1}{S^2}\mathfrak{B}_2 + \mathfrak{B}_3 - \frac{1}{S^2}\mathfrak{B}_4 + \mathfrak{B}_5\right\}, \qquad \text{(B.28)}
\end{aligned}
$$

where each $\mathfrak{B}_j, j = 1,2,3,4$ and 5, represents a square bracket inside the curly parentheses in (B.27) in the correct sequential order. We evaluate these $\mathfrak{B}_j$ one by one below.

Lemma B.3. *We have*

$$\mathfrak{B}_1 - \frac{1}{S^2}\mathfrak{B}_2 = 4ma^2\omega_0^2. \qquad \text{(B.29)}$$

Proof. Note the following pairs of cancellations:

$$\langle a(1)|H_1|a(1)\rangle - \frac{\langle b(1)|H_1|a(1)\rangle\langle b(2)|a(2)\rangle}{S^2} = 0, \tag{B.30}$$

$$\langle b(2)|H_2|b(2)\rangle - \frac{\langle a(2)|H_2|b(2)\rangle\langle b(1)|a(1)\rangle}{S^2} = 0, \tag{B.31}$$

because

$$H_1|a(1)\rangle = E_0|a(1)\rangle$$

as $|a(1)\rangle$ is the ground state of H_1 and E_0 is the ground state energy (cf. (B.17) with $n_+^{(1)} = n_-^{(1)} = 0$ therein) and so

$$\begin{aligned}\text{left-hand side of (B.30)} &= E_0\langle a(1)|a(1)\rangle - \frac{E_0\langle b(1)|a(1)\rangle\langle b(2)|a(2)\rangle}{S^2} \\ &= E_0 - \frac{E_0 \cdot S \cdot S}{S^2} = 0.\end{aligned}$$

Similarly,

$$H_2|b(2)\rangle = E_0|b(2)\rangle,$$

so (B.31) also holds.

For the two remaining terms in $\mathfrak{B}_1$, we have

$$\langle b(1)|H_1|b(1)\rangle + \langle a(2)|H_2|a(2)\rangle = 2\langle b(1)|H_1|b(1)\rangle \tag{B.32}$$

and by translation along the x_2-axis:

$$2\langle b(1)|H_1|b(1)\rangle = 2\langle b(2)|e^{\frac{i}{\hbar}[(\frac{eBa}{c})y_2 - 2ap_{x_2})]}H_2 e^{-\frac{i}{\hbar}[(\frac{eBa}{c})y_2 - 2ap_{x_2}]}|b(2)\rangle.$$

For $H_2(\boldsymbol{p}_2, \boldsymbol{r}_2)$ in (B.3), we have

$$\begin{aligned}&H_2(p_{x_2}, p_{y_2}, x_2, y_2) \\ &\quad = \frac{1}{2m}\left[\left(p_{x_2} + \frac{eB}{2c}y_2\right)^2 + \left(p_{y_2} - \frac{eBa}{2c} + \frac{e^2BE}{2mc\omega_0^2} - \frac{eB}{2c}x_{2+}\right)^2\right] \\ &\qquad + \frac{m\omega_0^2}{2}(x_{2+}^2 + y_2^2) - eE\left(\frac{eE}{2m\omega_0^2} - a\right),\end{aligned}$$

so

$$\begin{aligned}&e^{\frac{i}{\hbar}[(\frac{eBa}{c})y_2 - 2ap_{x_2}]}H_2(p_{x_2}, p_{y_2}, x_2, y_2)e^{-\frac{i}{\hbar}[(\frac{eBa}{c})y_2 - 2ap_{x_2}]} \\ &\qquad = H_2\left(p_{x_2}, p_{y_2} - \frac{eBa}{c}, x_2 - 2a, y_2\right) \\ &\qquad = \cdots \text{(substituting and simplifying)} \\ &\qquad = H_2(p_{x_2}, p_{y_2}, x_2, y_2) + \frac{m\omega_0^2}{2}(4a^2 - 4ax_{2+}).\end{aligned}$$

Therefore

$$(\text{B.32}) = 2\langle b(1)|H_2|b(1)\rangle = 2[\langle b(2)|H_2|b(2)\rangle - 2am\omega_0^2 \underbrace{\langle\, b(2)|x_{2+}|b(2)\rangle}_{\substack{=0 \text{ because the integrand} \\ \text{is an odd function of } x_{2+}}} + 2ma^2\omega_0^2]$$

$$= 2(E_0 + 2ma^2\omega_0^2). \tag{B.33}$$

The remaining terms in $-\frac{1}{S^2}\mathfrak{B}_2$ are

$$-\frac{1}{S^2}[\langle a(1)|H_1|b(1)\rangle S + \langle b(2)|H_2|a(2)\rangle S] = -\frac{S}{S^2}[\langle E_0 a(1)|b(1)\rangle + \langle E_0 b(2)|a(2)\rangle]$$

$$= -\frac{S}{S^2}\cdot 2E_0 S = -2E_0. \tag{B.34}$$

By adding (B.33) and (B.34), we obtain (B.29).

Lemma B.4. *We have*

$$\mathfrak{B}_3 - \frac{1}{S^2}\mathfrak{B}_4 = 2\hbar\omega_0\left[c\sqrt{b}\; e^{-bd^2} I_0(bd^2) - c\sqrt{b}\; e^{d^2(b-\frac{1}{b})} I_0\left(d^2\left(b-\frac{1}{b}\right)\right)\right]. \tag{B.35}$$

Proof. Note that by the symmetry $C(\boldsymbol{r}_1, \boldsymbol{r}_2) = C(\boldsymbol{r}_2, \boldsymbol{r}_1)$, we have

$$\begin{aligned}
\mathfrak{B}_3 &= 2\langle a(1)b(2)|C|a(1)b(2)\rangle \\
&= \int_{\mathbb{R}^2}\int_{\mathbb{R}^2} \overline{\Phi_0^{(1)}(x_1,y_1)\Phi_0^{(2)}(x_2,y_2)} \\
&\quad \times \frac{e^2}{\kappa|\overrightarrow{r}_1 - \overrightarrow{r}_2|}\Phi_0^{(1)}(x_1,y_1)\Phi_0^{(2)}(x_2,y_2)dx_1dy_1dx_2dy_2 \\
&= \left(\frac{m\Omega}{\pi\hbar}\right)^2 \frac{e^2}{\kappa}\int_{\mathbb{R}^2}\int_{\mathbb{R}^2} \frac{1}{|\overrightarrow{r}_1 - \overrightarrow{r}_2|} \\
&\quad \times e^{-\frac{m\Omega}{\hbar}\left[\left(x_1+a+\frac{eE}{m\omega_0^2}\right)^2+y_1^2+\left(x_2-a+\frac{eE}{m\omega_0^2}\right)^2+y_2^2\right]} dx_1dy_1dx_2dy_2.
\end{aligned} \tag{B.36}$$

Introduce the *center of mass coordinates*:

$$\begin{cases} \overrightarrow{R} = \dfrac{1}{2}(\overrightarrow{r}_1 + \overrightarrow{r}_2) & \text{(center of mass)}, \\ \overrightarrow{r} = \overrightarrow{r}_1 - \overrightarrow{r}_2 & \text{(relative coordinates)}, \end{cases} \tag{B.37}$$

$$\begin{cases} X = \dfrac{1}{2}(x_1+x_2),\ Y = \dfrac{1}{2}(y_1+y_2), \quad X = R\cos\Phi,\ Y = R\sin\Phi, \\ x = \dfrac{1}{2}(x_1-x_2),\ \ y = \dfrac{1}{2}(y_1-y_2), \quad x = r\cos\phi, \quad y = r\sin\phi. \end{cases} \tag{B.38}$$

This change of coordinates has the Jacobian equal to 1. Then, the integral in (B.36) becomes

$$
\begin{aligned}
(\text{B.36}) &= \left(\frac{m\Omega e}{\pi\hbar}\right)^2 \frac{1}{\kappa}\int_{\mathbb{R}^2}\int_{\mathbb{R}^2} \frac{1}{r} e^{-\frac{m\Omega}{\hbar}\left[X^2+xX+\frac{x^2}{4}+\left(a+\frac{eE}{m\omega_0^2}\right)(2X-x)+\left(a+\frac{eE}{m\omega_0^2}\right)^2+X^2-xX\right.} \\
&\quad \left.+\frac{x^2}{4}+\left(\frac{eE}{m\omega_0^2}-a\right)(2X-x)+\left(\frac{eE}{m\omega_0^2}-a\right)^2+Y^2+yY+\frac{y^2}{4}+Y^2-yY+\frac{y^2}{4}\right] r\,dr\,d\phi\,R\,dR\,d\Phi \\
&= \left(\frac{m\Omega e}{\pi\hbar}\right)^2 \frac{1}{\kappa}\int_0^{2\pi}\int_0^{\infty}\int_0^{2\pi}\int_0^{\infty} (dr\,d\phi)(R\,dR\,d\Phi) \\
&\quad \times\left\{e^{-\frac{m\Omega}{\hbar}\left[2R^2+\frac{r^2}{2}+2\left(a^2+\left(\frac{eE}{m\omega_0^2}\right)^2\right)+2ax+\frac{4eE}{m\omega_0^2}X^2\right]}\right\} \\
&= \left(\frac{m\Omega e}{\pi\hbar}\right)^2 \frac{1}{\kappa} e^{-\frac{2m\Omega}{\hbar}\left(a^2+\frac{e^2E^2}{m^2\omega_0^4}\right)} \int_0^{2\pi}\int_0^{\infty} R\,dR\,d\Phi\cdot e^{-\frac{m\Omega}{\hbar}\left[2R^2+\frac{4cE}{m\omega_0^2}X\right]} \\
&\quad \cdot\int_0^{2\pi}\int_0^{\infty} dr d\phi\cdot e^{-\frac{m\Omega}{\hbar}\left[\frac{r^2}{2}+2ar\cos\phi\right]} \\
&= \left(\frac{m\Omega e}{\pi\hbar}\right)^2 \frac{1}{\kappa} e^{-\frac{2m\Omega}{\hbar}\left(a^2+\frac{e^2E^2}{m^2\omega_0^4}\right)} \left\{\int_{-\infty}^{\infty} e^{-\frac{m\Omega}{\hbar}\left[2X^2+\frac{4eE}{m\omega_0^2}X\right]}\right. \\
&\quad \left.\times\left[\int_{-\infty}^{\infty} e^{-\frac{2m\Omega}{\hbar}Y^2}dY\right]dX\right\}\cdot \\
&\quad \cdot\left\{\int_0^{\infty} e^{-\frac{m\Omega}{2\hbar}r^2}\underbrace{\left[\int_0^{2\pi} e^{-\frac{2m\Omega a}{\hbar}r\cos\phi}\,d\phi\right]}_{(\mathcal{J}_1)}dr\right\}. \qquad (\text{B.39})
\end{aligned}
$$

We evaluate the integral $(\mathcal{J}_1)$ above by using the expansion

$$
\begin{aligned}
e^{-(\frac{2m\Omega a}{\hbar}r)\cos\phi} &= \sum_{m=-\infty}^{\infty}(-1)^m I_m\left(\frac{2m\Omega a}{\hbar}r\right)e^{im\phi} \\
&= I_0\left(\frac{2m\Omega a}{\hbar}r\right)+2\sum_{m=1}^{\infty} I_m\left(\frac{2m\Omega a}{\hbar}r\right)\cos(m\phi) \\
&\quad \text{[cf. Abramowitz and Stegun (Ref. 1, p. 376, Formula 9.6.34)]}
\end{aligned}
$$

$$
\begin{aligned}
(\mathcal{J}_1) &= \int_0^{2\pi}\left\{I_0\left(\frac{2m\Omega a}{\hbar}r\right)+2\sum_{m=1}^{\infty} I_m\left(\frac{2m\Omega a}{\hbar}r\right)\cos m\phi\right\}d\phi \\
&= 2\pi I_0\left(\frac{2m\Omega a}{\hbar}r\right).
\end{aligned}
$$

Substituting $(\mathcal{J}_1)$ into (B.39) above and continuing, we obtain

$$(\text{B.36}) = \left(\frac{m\Omega e}{\pi\hbar}\right)^2 \frac{1}{\kappa} e^{-\frac{2m\Omega}{\hbar}\left(a^2+\frac{e^2E^2}{m^2\omega_0^4}\right)} \cdot e^{\frac{2m\Omega}{\hbar}\frac{e^2E^2}{m^2\omega_0^4}} \cdot \underbrace{\int_{-\infty}^{\infty} e^{-\frac{2m\Omega}{\hbar}\left(X+\frac{eE}{m\omega_0^2}\right)^2} dX}_{\left(\frac{\pi\hbar}{2m\Omega}\right)^{1/2}}$$

$$\cdot \underbrace{\int_{-\infty}^{\infty} e^{-\frac{2m\Omega}{\hbar}Y^2} dY}_{\left(\frac{\pi\hbar}{2m\Omega}\right)^{1/2}} \cdot 2\pi \underbrace{\int_0^{\infty} e^{-\frac{m\Omega}{2\hbar}r^2} I_0\left(\frac{2m\Omega a}{\hbar}r\right) dr}_{(\mathcal{J}_2)}.$$

To evaluate the integral $(\mathcal{J}_2)$, we use

$$\int_0^{\infty} e^{-ax^2} I_\nu(bx)dx = \frac{1}{2}\sqrt{\frac{\pi}{a}} e^{\frac{b^2}{8a}} I_{\frac{1}{2}\nu}\left(\frac{b^2}{8a}\right) \quad (\text{for Re } \nu > -1, \text{ Re } a > 0)$$

[cf. Abramowitz and Stegun (Ref. 1, p. 487, Formula 11.4.31)].

Then

$$(\mathcal{J}_2) = \frac{1}{2}\sqrt{\frac{2\hbar\pi}{m\Omega}} e^{\frac{m\Omega a^2}{\hbar}} I_0\left(\frac{m\Omega a^2}{\hbar}\right).$$

Therefore, we have arrived at

$$\begin{aligned}\mathfrak{B}_3 &= 2\langle a(1)b(2)|C|a(1)b(2)\rangle = 2\left(\frac{\pi m\Omega}{2\hbar}\right)^{1/2} \frac{e^2}{\kappa} e^{-\frac{m\Omega a^2}{\hbar}} I_0\left(\frac{m\Omega a^2}{\hbar}\right) \\ &= 2\hbar\omega_0 c\sqrt{b}\; e^{-bd^2} I_0(bd^2); \quad \left(\text{with } c = \frac{e^2}{\kappa}\frac{1}{\hbar\omega_0}\sqrt{\frac{\pi m\omega_0}{2\hbar}}, \text{ cf. (3.9)}\right). \qquad (\text{B.40})\end{aligned}$$

Next, we proceed to evaluate integral in $\mathfrak{B}_4$:

$$\begin{aligned}\mathfrak{B}_4 &= \langle a(1)b(2)|C|a(2)b(1)\rangle + \langle a(2)b(1)|C|a(1)b(2)\rangle \\ &= 2\ \text{Re}\langle a(1)b(2)|C|a(2)b(1)\rangle \\ &= \cdots \text{ (similar to (B.36)–(B.39), using the center of mass coordinates} \\ &\quad \text{(B.37) and (B.38))} \\ &= 2\ \text{Re}\left(\frac{m\Omega e}{\pi\hbar}\right)^2 \frac{1}{\kappa}\int_0^{2\pi}\int_0^{2\pi}\int_0^{\infty}\int_0^{\infty} \frac{1}{r}\exp\left\{i\frac{eBa}{\hbar c}y - \frac{m\Omega}{\hbar}\left[\left(\frac{2X+x}{2}\right)^2\right.\right. \\ &\quad \left.\left. + \left(\frac{2X-x}{2}\right)^2 + 2a^2 + \left(\frac{2Y+y}{2}\right)^2 + \left(\frac{2Y-y}{2}\right)^2\right]\right\} r\,dr\,R\,dR\cdot d\phi\,d\Phi \\ &= 2\ \text{Re}\left(\frac{m\Omega e}{\pi\hbar}\right)^2 \frac{1}{\kappa} e^{-\frac{2m\Omega a^2}{\hbar}} \int_0^{2\pi}\int_0^{2\pi}\int_0^{\infty}\int_0^{\infty} \\ &\quad \times \exp\left\{\frac{ieBa}{\hbar c}y - \frac{m\Omega}{\hbar}\left[2X^2 + 2Y^2 + \frac{x^2}{2} + \frac{y^2}{2}\right]\right\}\cdot \\ &\quad \cdot dr\,R\,dR\,d\phi\,d\Phi\end{aligned}$$

$$= 2\ \mathrm{Re}\left(\frac{m\Omega e}{\phi\hbar}\right)^2 \frac{1}{\kappa} e^{-\frac{2m\Omega a^2}{\hbar}} \int_{-\infty}^{\infty} e^{-\frac{2m\Omega}{\hbar}X^2} dX \cdot \int_{-\infty}^{\infty} e^{-\frac{2m\Omega}{\hbar}Y^2} dY$$
$$\cdot \int_0^{\infty} e^{-\frac{m\Omega}{2\hbar}r^2} \underbrace{\left[\int_0^{2\pi} e^{\frac{ieBa}{\hbar c} r\sin\phi} d\phi\right]}_{(\mathcal{J}_3)} dr$$
$$= 2\ \mathrm{Re}\left(\frac{m\Omega e}{\pi\hbar}\right)^2 \frac{1}{\kappa} e^{-\frac{2m\Omega a^2}{\hbar}} \cdot \left(\frac{\pi\hbar}{2m\Omega}\right)^{1/2} \cdot \left(\frac{\pi\hbar}{2m\Omega}\right)^{1/2} \underbrace{\int_0^{\infty} e^{-\frac{m\Omega}{2\hbar}r^2} (\mathcal{J}_3) dr}_{(\mathcal{J}_4)},$$

where

$$(\mathcal{J}_3) = \int_0^{2\pi} e^{\frac{ieBa}{\hbar c} r\sin\phi} d\phi = J_0\left(\frac{eBa}{\hbar c} r\right) \cdot 2\pi$$

[cf. Abramowitz and Stegun (Ref. 1, p. 360, Formula 9.1.18)]

and

$$(\mathcal{J}_4) = 2\pi \int_0^{\infty} e^{-\frac{m\Omega}{2\hbar}r^2} J_0\left(\frac{eBa}{\hbar c} r\right) dr$$
$$= 2\pi \sqrt{\frac{\hbar\pi}{2m\Omega}} e^{-(\frac{eBa}{\hbar c})^2 \frac{\hbar}{4m\Omega}} \cdot I_0\left(\left(\frac{eBa}{\hbar c}\right)^2 \frac{\hbar}{4m\Omega}\right)$$

[cf. Gradshteyn and Ryzhik (Ref. 19, p. 732, Formula 6.618(1))].

Therefore, we have arrived at

$$\mathfrak{B}_4 = 2\ \mathrm{Re}\langle a(1)b(2)|C|a(2)b(1)\rangle$$
$$= 2\ \mathrm{Re}\left(\frac{m\Omega}{\hbar}\right)^{1/2} \sqrt{\frac{\pi}{2}} \frac{e^2}{\kappa} e^{-\frac{2m\Omega}{\hbar}a^2 - \frac{e^2B^2a^2}{4\hbar c^2 m\Omega}} I_0\left(\frac{e^2B^2a^2}{4\hbar c^2 m\Omega}\right)$$
$$= 2\hbar\omega_0 c\sqrt{b}\ e^{-2bd^2} e^{-d^2(b-\frac{1}{b})} I_0\left(d^2\left(b - \frac{1}{b}\right)\right). \tag{B.41}$$

Using S in (B.24), we obtain from (B.40) and (B.41) that $\mathfrak{B}_3 - (1/S^2)\mathfrak{B}_4$ is indeed equal to (B.35).

Finally, we evaluate $\mathfrak{B}_5$.

Lemma B.5. *We have*

$$\mathfrak{B}_5 = -4m\omega_0^2 a^2 + 2 \cdot \left(\frac{m\omega_0^2}{2}\right) \left[\frac{3\hbar}{2m\Omega} + 3\left(\frac{eE}{m\omega_0^2}\right)^2 + \frac{3}{2}a^2\right]. \tag{B.42}$$

Proof. First, we want to show that

$$\langle a(1)b(2)|W|a(1)b(2)\rangle + \langle a(2)b(1)|W|a(2)b(1)\rangle$$
$$= 2\langle a(1)b(2)|W|a(1)b(2)\rangle - 4m\omega_0^2 a^2. \tag{B.43}$$

The first term in $\mathfrak{B}_5$ [and on the left-hand side of (B.43)] satisfies

$$\begin{aligned}\langle a(1)b(2)|W|a(1)b(2)\rangle &= \langle a(1)|W_1|a(1)\rangle + \langle b(2)|W_2|b(2)\rangle \quad \text{[see (B.4) and (B.4)]}\\ &= \langle b(1)|e^{\frac{i}{\hbar}\left(\frac{eBa}{c}y_1-2ap_{x_1}\right)}W_1 e^{-\frac{i}{\hbar}\left(\frac{eBa}{c}y_1-2ap_{x_1}\right)}|b(1)\rangle\\ &\quad + \langle a(2)|e^{-\frac{i}{\hbar}\left(\frac{eBa}{c}y_2-2ap_{x_2}\right)}W_2 e^{\frac{i}{\hbar}\left(\frac{eBa}{c}y_2-2ap_{x_2}\right)}|a(2)\rangle.\end{aligned} \tag{B.44}$$

But

$$W_1(x) = \frac{m\omega_0^2}{2}\left[\frac{1}{4a^2}(x^2-a^2)^2-(x+a)^2\right],$$

so

$$\begin{aligned}&e^{\frac{i}{\hbar}\left(\frac{eBa}{c}y_1-2ap_{x_1}\right)}W_1(x_1)e^{-\frac{i}{\hbar}\left(\frac{eBa}{c}y_1-2ap_{x_1}\right)}\\ &\quad = W_1(x_1-2a)\\ &\quad = \frac{m\omega_0^2}{2}\left[\frac{1}{4a^2}((x_1-2a)^2-a^2)^2-(x_1-2a+a)^2\right]\\ &\quad = \cdots(\text{expanding and regrouping terms})\\ &\quad = W_1(x_1)+\frac{m\omega_0^2}{2}\left[4ax_1-\frac{2}{a}(x_1-a)^3\right].\end{aligned} \tag{B.45}$$

Similarly, for W_2 given in (B.4),

$$\begin{aligned}&e^{-\frac{i}{\hbar}\left(\frac{eBa}{c}y_2-2ap_{x_2}\right)}W_2(x_2)e^{\frac{i}{\hbar}\left(\frac{eBa}{c}y_2-2ap_{x_2}\right)}\\ &\quad = W_2(x_2+2a)\\ &\quad = W_2(x_2)+\frac{m\omega_0^2}{2}\left[-4ax_2+\frac{2}{a}(x_2+a)^3\right].\end{aligned} \tag{B.46}$$

Thus, continuing from (B.44) using (B.45) and (B.46), we have

$$\begin{aligned}(\text{B.44}) &= \langle b(1)|W_1|b(1)\rangle + \langle b(1)|\frac{m\omega_0^2}{2}\left[4ax_1-\frac{2}{a}(x_1-a)^3\right]|b(1)\rangle\\ &\quad + \langle a(2)|W_2|a(2)\rangle + \langle a(2)|\frac{m\omega_0^2}{2}\left[-4ax_2+\frac{2}{a}(x_2+a)^3\right]|a(2)\rangle\\ &= \langle b(1)a(2)|W|b(1)a(2)\rangle + 2m\omega_0^2 a[\langle b(1)|x_1|b(1)\rangle - \langle a(2)|x_2|a(2)\rangle]\\ &\quad + \frac{m\omega_0^2}{a}[\langle a(2)|(x_2+a)^3|a(2)\rangle - \langle b(1)|(x_1-a)^3|b(1)\rangle]\\ &= \langle b(1)a(2)|W|b(1)a(2)\rangle + 2m\omega_0^2 a\Bigg[\langle b(1)|(x_1)_+ + a - \frac{eE}{m\omega_0^2}|b(1)\rangle\\ &\quad - \langle a(2)|(x_2)_- - a - \frac{eE}{m\omega_0^2}|a(2)\rangle\Bigg]\\ &\quad + \frac{m\omega_0^2}{a}\left[\langle a(2)|\left((x_2)_- - \frac{eE}{m\omega_0^2}\right)^3|a(2)\rangle - \langle b(1)|\left((x_1)_+ - \frac{eE}{m\omega_0^2}\right)^3|b(1)\rangle\right]\\ &\quad \left(\text{where, recall that } x_+ = x-a+\frac{eE}{m\omega_0^2} \text{ and } x_- = x+a+\frac{eE}{m\omega_0^2}\right)\end{aligned}$$

$$
\begin{aligned}
&= \langle b(1)a(2)|W|b(1)a(2)\rangle + 4m\omega_0^2 a^2 \\
&\quad + \frac{m\omega_0^2}{a}\left[\langle a(2)|(x_2)_-^3 - \frac{3eE}{m\omega_0^2}(x_2)_-^2 + 3\left(\frac{eE}{m\omega_0^2}\right)^2(x_2)_- - \left(\frac{eE}{m\omega_0}\right)^3|a(2)\rangle\right. \\
&\quad \left. - \langle b(1)|(x_1)_+^3 - 3\frac{eE}{m\omega_0^2}(x_1)_+^2 + 3\left(\frac{eE}{m\omega_0^2}\right)^2(x_1)_+ - \left(\frac{eE}{m\omega_0}\right)^3|b(1)\rangle\right] \\
&= \langle b(1)a(2)|W|b(1)a(2)\rangle + 4m\omega_0^2 a^2. \qquad \text{(B.47)}
\end{aligned}
$$

By (B.44) and (B.47), we have confirmed (B.43). So our objective now is to evaluate $\langle a(1)b(2)|W|a(1)b(2)\rangle$:

$$\langle a(1)b(2)|W|a(1)b(2)\rangle = \langle a(1)|W_1|a(1)\rangle + \langle b(2)|W_2|b(2)\rangle; \qquad \text{(B.48)}$$

$$
\begin{aligned}
\langle a(1)|W_1|a(1)\rangle &= \frac{m\Omega}{\pi\hbar}\int_{-\infty}^{\infty}\int_{-\infty}^{\infty} e^{-\frac{m\Omega}{\hbar}\left[\left(x_1+a+\frac{eE}{m\omega_0^2}\right)^2+y_1^2\right]} \\
&\quad \cdot \frac{m\omega_0^2}{2}\left[\frac{1}{4a^2}(x_1^2-a^2)^2-(x_1+a)^2\right]dx_1dy_1 \equiv f(a); \qquad \text{(B.49)}
\end{aligned}
$$

$$
\begin{aligned}
\langle b(2)|W_2|b(2)\rangle &= \frac{m\Omega}{\pi\hbar}\int_{-\infty}^{\infty}\int_{-\infty}^{\infty} e^{-\frac{m\Omega}{\hbar}\left[\left(x_2-a+\frac{eE}{m\omega_0^2}\right)^2+y_2^2\right]} \\
&\quad \cdot \frac{m\omega_0^2}{2}\left[\frac{1}{4a^2}(x_2^2-a^2)^2-(x_2-a)^2\right]dx_2dy_2. \qquad \text{(B.50)}
\end{aligned}
$$

By comparing (B.49) and (B.50), we see that if the outcome of (B.49) is $f(a)$ (with all the parameters other than a being fixed), then the outcome of (B.50) will be $f(-a)$.

Similarly,

$$
\begin{aligned}
\langle a(1)|W_1|b(1)\rangle &= \frac{m\Omega}{\pi\hbar}\int_{-\infty}^{\infty}\int_{-\infty}^{\infty} e^{\frac{i}{\hbar}\frac{eBa}{c}y_1} e^{-\frac{m\Omega}{\hbar}\left[\left(x_1+\frac{eE}{m\omega_0^2}\right)^2+a^2+y_1^2\right]} \\
&\quad \cdot \frac{m\omega_0^2}{2}\left[\frac{1}{4a^2}(x_1^2-a^2)^2-(x_1+a)^2\right]dx_1dy_1 \equiv g(a), \qquad \text{(B.51)}
\end{aligned}
$$

then

$$
\begin{aligned}
\langle b(2)|W_2|a(2)\rangle &= \frac{m\Omega}{\pi\hbar}\int_{-\infty}^{\infty}\int_{-\infty}^{\infty} e^{-\frac{i}{\hbar}\frac{eBa}{c}y_2} e^{-\frac{m\Omega}{\hbar}\left[\left(x_2+\frac{eE}{m\omega_0^2}\right)^2+a^2+y_2^2\right]} \cdot \\
&\quad \cdot \frac{m\omega_0^2}{2}\left[\frac{1}{4a^2}(x_2^2-a^2)^2-(x_2-a)^2\right]dx_2dy_2 = g(-a). \qquad \text{(B.52)}
\end{aligned}
$$

By translating $x \mapsto x - a - \frac{eE}{m\omega_0^2}$, we have

$$\langle a(1)|W_1|a(1)\rangle = \text{(B.49)} = \frac{m\Omega}{\pi\hbar}\left[\int_{-\infty}^{\infty} e^{-\frac{m\Omega}{\hbar}y^2}dy\right] \times \left[\int_{-\infty}^{\infty} e^{-\frac{m\Omega}{\hbar}x^2} W_1\left(x - a - \frac{eE}{m\omega_0^2}\right)dx\right]. \quad \text{(B.53)}$$

Here

$$W_1\left(x - a - \frac{eE}{m\omega_0^2}\right) = W_1(x - a - \beta) \quad \left(\beta \equiv \frac{eE}{m\omega_0^2}\right) \quad \text{(B.54)}$$

$$= \frac{m\omega_0^2}{2}\left\{\frac{1}{4a^2}[(x-a-\beta)^2 - a^2]^2 - (x-\beta)^2\right\}$$

$$= \frac{m\omega_0^2}{2}\left[\frac{1}{4a^2}(x-\beta)^4 - \frac{1}{a}(x-\beta)^3\right]$$

$$= \frac{m\omega_0^2}{2}\left[\frac{1}{4a^2}x^4 - \left(\frac{\beta}{a^2} + \frac{1}{a}\right)x^3 + \left(\frac{3}{2}\frac{\beta^2}{a^2} + \frac{3\beta}{a}\right)x^2 - \left(\frac{\beta^3}{a^2} + \frac{3\beta^2}{a}\right)x + \left(\frac{\beta^4}{4a^2} + \frac{\beta^3}{a}\right)\right]. \quad \text{(B.55)}$$

Recalling the formulas for Gaussian integrals

$$\int_{-\infty}^{\infty} x^{2n} e^{-\alpha x^2}dx = -\left(\frac{\partial}{\partial\alpha}\right)^n \int_{-\infty}^{\infty} e^{-\alpha x^2}dx = \left(-\frac{\partial}{\partial\alpha}\right)^n \sqrt{\frac{\pi}{\alpha}}$$

$$= \left[\prod_{k=1}^{n}\left(\frac{1}{2} + k - 1\right)\right]\left(\frac{1}{\alpha^n}\sqrt{\frac{\pi}{\alpha}}\right), \quad \text{for } n = 1, 2, \ldots, \quad \text{(B.56)}$$

$$\int_{-\infty}^{\infty} x^{2n+1} e^{-\alpha x^2}\, dx = 0, \quad \text{for } n = 0, 1, 2, \ldots, \quad \text{(B.57)}$$

from (B.53), (B.55)–(B.57), we obtain

$$\langle a(1)|W_1|a(1)\rangle = \frac{m\Omega}{\pi\hbar}\left(\frac{\pi\hbar}{m\Omega}\right)^{1/2}\left(\frac{m\omega_0^2}{2}\right) \cdot \left[\frac{1}{4a^2}\frac{\partial^2}{\partial\alpha^2} - \left(\frac{3\beta^2}{2a^2} + \frac{3\beta}{a}\right)\frac{\partial}{\partial\alpha} + \left(\frac{\beta^4}{4a^2} + \frac{\beta^3}{a}\right)\right]\left(\sqrt{\frac{\pi}{\alpha}}\right)$$

(where $\alpha \equiv m\Omega/\hbar$)

$$= \frac{m\Omega}{\pi\hbar}\left(\frac{\pi\hbar}{m\Omega}\right)^{1/2}\frac{m\omega_0^2}{2}\left(\frac{\pi\hbar}{m\Omega}\right)^{1/2} \cdot \left[\frac{1}{4a^2}\frac{3\hbar^2}{4m^2\Omega^2} + \frac{1}{2}\left(\frac{3\beta^2}{2a^2} + \frac{3\beta}{a}\right)\frac{\hbar}{m\Omega} + \frac{\beta^4}{4a^2} + \frac{\beta^3}{a}\right]$$

$$= \frac{m\omega_0^2}{2}\left[\frac{3\hbar^2}{16m^2\Omega^2a^2} + \left(\frac{3\beta^2}{4a^2} + \frac{3\beta}{2a}\right)\frac{\hbar}{m\Omega} + \frac{\beta^4}{4a^2} + \frac{\beta^3}{a}\right]$$
$$= f(a) \quad \text{[cf. (B.49)]}.$$

Then, $\langle b(2)|W_2|b(2)\rangle = f(-a)$ and so from (B.48), we obtain

$$\langle a(1)b(2)|W|a(2)b(1)\rangle = \frac{m\omega_0^2}{2}\left[\frac{3\hbar^2}{8m^2\Omega^2a^2} + \frac{3\beta^2\hbar}{2a^2m\Omega} + \frac{\beta^4}{2a^2}\right]. \tag{B.58}$$

Next, repeat similar procedures,

$$\begin{aligned}
\text{(B.51)} &= \frac{m\Omega}{\pi\hbar}e^{-\frac{m\Omega}{\hbar}a^2}\left[\int_{-\infty}^{\infty} e^{\frac{i}{\hbar}\frac{eBa}{c}y - \frac{m\Omega}{\hbar}y^2}\,dy\right]\left[\int_{-\infty}^{\infty} e^{-\frac{m\Omega}{\hbar}x^2}W_1(x-\beta)dx\right] \\
&= \frac{m\Omega}{\pi\hbar}e^{-\frac{m\Omega}{\hbar}a^2}\left[\int_{-\infty}^{\infty} e^{-\frac{m\Omega}{\hbar}(y - i\frac{eBa}{2m\Omega c})^2 - \frac{m\Omega}{\hbar}\frac{e^2B^2a^2}{4m^2\Omega^2c^2}}dy\right] \\
&\quad \cdot \int_{-\infty}^{\infty} e^{-\frac{m\Omega}{\hbar}x^2}\cdot\frac{m\omega_0^2}{2}\left[\frac{1}{4a^2}(x-\beta+a)^4 - \frac{1}{a}(x-\beta+a)^3\right]dx \\
&= \left(\frac{m\Omega}{\pi\hbar}\right)e^{-\frac{m\Omega}{\hbar}a^2 - \frac{e^2B^2a^2}{4\hbar m\Omega c^2}}\left(\frac{\pi\hbar}{m\Omega}\right)^{1/2}\cdot\left(\frac{\pi\hbar}{m\Omega}\right)^{1/2}\cdot\frac{m\omega_0^2}{2} \\
&\quad \cdot \left\{\frac{3\hbar^2}{16m^2\Omega^2a^2} + \left[\frac{3(\beta-a)^2}{4a^2} + \frac{3(\beta-a)}{2a}\right]\right. \\
&\quad \left.\cdot\ \frac{\hbar}{m\Omega} + \frac{(\beta-a)^4}{4a^2} + \frac{(\beta-a)^3}{a}\right\} = g(a).
\end{aligned} \tag{B.59}$$

Therefore,

$$\begin{aligned}
&\langle a(1)b(2)|W|a(2)b(1)\rangle \\
&\quad = \langle a(1)|W_1|b(1)\rangle\langle b(2)|a(2)\rangle + \langle a(1)|b(1)\rangle\cdot\langle b(2)|W_2|a(2)\rangle \\
&\quad = S[\langle a(1)|W_1|b(1)\rangle + \langle b(2)|W_2|a(2)\rangle] \\
&\quad = S[g(a) + g(-a)] \qquad \text{[by (B.52)]} \\
&\quad = S\cdot e^{-\frac{a^2}{\hbar}\left(m\Omega + \frac{e^2B^2}{4m\Omega c^2}\right)}\frac{m\omega_0^2}{2}\left[\frac{3\hbar^2}{8m^2\Omega^2a^2} + \left(\frac{3\beta^2}{2a^2} + \frac{3}{2} - 3\right)\frac{\hbar}{m\Omega}\right. \\
&\qquad \left. + \frac{\beta^4}{2a^2} + 3\beta^2 + \frac{a^2}{2} - 6\beta^2 - 2a^2\right] \quad \text{[from (B.58) and (B.52)]}.
\end{aligned}$$

But the factor $e^{-\frac{a^2}{\hbar}\left(m\Omega + \frac{e^2B^2}{4m\Omega c^2}\right)}$ behind S is just S itself from (B.24). Thus,

$$\begin{aligned}
&\frac{1}{S^2}\langle a(1)b(2)|W|a(2)b(1)\rangle \\
&\quad = \frac{m\omega_0^2}{2}\left[\frac{3\hbar^2}{8m^2\Omega^2a^2} + \frac{3}{2}\left(\frac{\beta^2}{a^2} - 1\right)\frac{\hbar}{m\Omega} + \frac{\beta^4}{2a^2} - 3\beta^2 - \frac{3}{2}a^2\right].
\end{aligned} \tag{B.60}$$

Summarizing (B.43), (B.58) and (B.60), we have

$$\begin{aligned}\mathfrak{B}_5 &= 2\langle a(1)b(2)|W|a(1)b(2)\rangle - 4m\omega_0^2 a^2 - 2\ \mathrm{Re}\cdot\frac{1}{S^2}\langle a(1)b(2)|W|a(2)b(1)\rangle \\ &= -4m\omega_0^2 a^2 + 2\cdot\left(\frac{m\omega_0^2}{2}\right)\left(\frac{3\hbar}{2m\Omega} + 3\beta^2 + \frac{3}{2}a^2\right).\end{aligned}$$

This is (B.42).

We can now combine all the preceding lemmas and finally obtain the following.

Theorem B.1. *The exchange energy is given by*

$$\begin{aligned}J &= \langle\Psi_-|H_{\mathrm{orb}}|\Psi_-\rangle - \langle\Psi_+|H_{\mathrm{orb}}|\Psi_+\rangle \\ &= (3.4).\end{aligned}$$

Proof. We only need note that with S given in (B.24), we have

$$\frac{S^2}{1-S^4} = \frac{1}{S^{-2}-S^2} = \frac{1}{2\sinh\left(2d^2\left(2b-\frac{1}{b}\right)\right)}.$$

Thus, the coefficient outside the parentheses in (B.28) is determined as above. We now collect all the terms in (B.29), (B.35), and (B.42), noting the cancellation of the terms $4ma^2\omega_0^2$ and $-4ma^2\omega_0^2$ in (B.28) and (B.42), and then simplify (just a little). We then obtain (3.4).

Acknowlegments

G. Chen is spported in part by a DARPA QuIST grant, and by TITF grant from Texas A&M University. A. Neogi is supported in part by a Faculty Research Grant from the University of North Texas.

References

1. M. Abramowitz and I. Stegun, *Handbook of Mathematical Functions*, 9th printing (Dover, New York, 1970).
2. J. Ahopelto, Emerging nanopatterning methods, in *Proc. Int. Conf. Ultimate Lithography and Nanodevice Engineering*, Agelonde, France (2004).
3. M. N. Baibich, J. M. Broto, A. Fert, F. Nguyen Van Dau, F. Petroff, P. Eitenne, G. Creuzet, A. Friederich and J. Chazelas, Giant magnetoresistance of (001)Fe/(001)Cr magnetic superlattices, *Phys. Rev. Lett.* **61** (1988) 2472.
4. P. Bhattacharya *et al.*, In(Ga)As/GaAs self-organized quantum dot lasers: DC and small-signal modulation properties, *IEEE Trans. Electron Devices* **46** (1999) 871–883.
5. D. Birkedal, K. Leosson and J. M. Hvam, Long lived coherence in self-assembled quantum dots, *Phys. Rev. Lett.* **87** (2001) 227401.
6. N. H. Bonadeo, G. Chen, D. Gammon, D. S. Katzer, D. Park and D. G. Steel, Nonlinear nano-optics: Probing one exciton at a time, *Phys. Rev. Lett.* **81** (1998) 2759–2762.

7. K. R. Brown, D. A. Lidar and K. B. Whaley, Quantum computing with quantum dots on quantum linear supports, *Phys. Rev. A* **65** (2001) 012307.
8. J. L. Brylinski and R. Brylinski, Universal quantum gates, in *Mathematics of Quantum Computation*, eds. R. Brylinski and G. Chen (Chapman & Hall/CRC Press, Boca Raton, FL, 2002), pp. 101–116.
9. G. Burkard, H.-A. Engel and D. Loss, Spintronics, quantum computing and quantum communications in quantum dots, in *Fundamentals of Quantum Information*, ed. W. D. Heiss (Springer-Verlag, Berlin and Heidelberg, 2002), pp. 241–265.
10. G. Burkard, D. Loss and D. DiVincenzo, Coupled quantum dots as quantum gates, *Phys. Rev. B* **59** (1999) 2070–2078.
11. G. Chen, D. A. Church, B.-G. Englert and M. S. Zubairy, Mathematical models of contemporary elementary quantum computing devices, in *Quantum Control: Mathematical and Numerical Challenges*, eds. A. D. Bandrauk, M. C. Delfour and C. Le Bris, CRM Proc. & Lecture Notes, Vol. 33 (American Mathematical Society, Providence, 2003), pp. 79–117.
12. C. Darwin, The diamagnetism of the free electron, *Proc. Cambridge Phil. Soc.* **27** (1930) 86.
13. D. P. DiVincenzo, The physical implementation of quantum computation, *Fortschr. Phys.* **48** (2000) 771.
14. R. J. Elliot, *Phy. Rev.* **108** (1957) 1348.
15. V. Fock, Bermerkung zur Quantelung des harmonischen Oszillators in Magnetfeld, *Zeit. Physik* **47** (1928) 446.
16. W. Franz, *Z. Naturforsch. A* **13** (1958) 484.
17. J. M. Gerard and B. Gayral, Strong Purcell effect for InAs quantum boxes in three-dimensional solid-state microcavities, *J. Lightwave Technol.* **17** (1999) 2089–2095.
18. L. Goldstein, F. Glas, J. Y. Marzin, M. N. Charasse and G. Le Roux, *Appl. Phys. Lett.* **47** (1985) 1099.
19. I. S. Gradshteyn and I. M. Ryzhik, *Table of Integrals, Series and Products*, 6th edn. (Academic Press, New York, 2000).
20. J. M. Kikkawa and D. D. Awschalom, Resonant spin amplification in n-type GaAs, *Phys. Rev. Lett.* **80** (1998) 4313.
21. I. L. Krestnikov, N. A. Maleev, A. V. Sakharov, A. R. Kovsh, A. E. Zhukov, A. F. Tsatsul'nikov, V. M. Ustinov, Zh. I. Alferov, N. N. Ledentsov, D. Bimberg and J. A. Lott, 1.3 m resonant-cavity InGaAs/GaAs quantum dot light-emitting devices, *Semicond. Sci. Technol.* **16** (2001) 844–848.
22. A. A. Lagatsky, E. U. Rafailov, W. Sibbett, D. A. Livshits, A. E. Zhukov and V. M. Ustinov, Quantum-dot-based saturable absorber with p-n junction for mode-locking of solid-state lasers, *IEEE Photonics Tech. Lett.* **17** (2005) 294–296.
23. R. Landauer, *Proc. R. Soc. London Ser. A* **454** (1998) 305.
24. L. Landin *et al.*, Optical studies of individual InAs quantum dots in GaAs: Few-particle effects, *Science* **280** (1998) 262–264.
25. X. Li, Y. Wu, D. Steel, D. Gammon, T. H. Stievater, D. S. Katzer, D. Park, C. Piermarocchi and L. J. Sham, An all-optical quantum gate in a semiconductor quantum dot, *Science* **301** (2003) 809–811.
26. H. K. Lo and S. Braunstein (eds.) *Fortschr. Phys.* **48** (2000). [Special issue on *Experimental Proposals for Quantum Computation*].
27. D. Loss and D. DiVincenzo, Quantum computation with quantum dots, *Phys. Rev. A* **57** (1998) 120–126.

28. P. Michler, A. Imamoglu, M. D. Mason, P. J. Carson, G. F. Strouse and S. K. Buratto, Quantum correlation among photons from a single quantum dot at room temperature, *Nature* **406** (2000) 968.
29. D. A. B. Miller *et al.*, *Phys. Rev. Lett.* **53** (1984) 2173.
30. A. Neogi, B. P. Gorman, H. Morkoç, T. Kawazoe and M. Ohtsu, Near-field optical spectroscopy and microscopy of self-assembled GaN/AlN nanostructures, *Appl. Phys. Lett.* **86** (2005) 43103.
31. A. Neogi, H. Morkoç, T. Kuroda, A. Tackeuchi, T. Kawazoe and M. Ohtsu, Exciton localization in vertically and laterally coupled GaN/AlN quantum dots, *Nano Lett.* **5** (2005) 209–212.
32. A. Neogi, H. Yoshida, T. Mozume, N. Georgiev and O. Wada, Intersubband transitions and ultrafast all-optical modulation using multiple InGaAs-AlAsSb-InP coupled double-quantum-well structures, *IEEE J. Sel. Top. Quant. Elect.* **7** (2001) 710–717.
33. C. Piermarocchi, P. Chen, Y. S. Dale and L. J. Sham, Theory of fast quantum control of exciton dynamics in semiconductor quantum dots, *Phys. Rev. B* **65** (2002) 075307.
34. C. Piermarocchi, P. Chen, L. J. Sham and D. G. Steel, Optical RKKY interaction between charged semiconductor quantum dots, *Phys. Rev. Lett.* **89** (2002) 167402.
35. A. Rauschenbeutel, G. Nogues, S. Osnaghi, P. Bertet, M. Brune, J. M. Raimond and S. Haroche, Coherent operation of a tunable quantum phase gate in cavity QED, *Phys. Rev. Lett.* **83** (1999) 5166–5169.
36. M. S. Sherwin, A. Imamoglu and T. Montroy, Quantum computation with quantum dots and terahertz cavity quantum electrodynamics, *Phys. Rev. A* **60** (1999) 3508–3514.
37. L. J. Sham and T. M. Rice, Many-particle derivation of the effective-mass equation for the wannier exciton, *Phys. Rev.* **144** (1966) 708–714.
38. J. C. Slater, *Quantum Theory of Molecules and Solids*, Vol. 1 (McGraw-Hill, New York, 1963).
39. G. S. Solomon, M. Pelton and Y. Yamamoto, Single-mode spontaneous emission from a single quantum dot in a three-dimensional microcavity, *Phys. Rev. Lett.* **86** (2001) 3903.
40. T. H. Stievater, X. Li, D. G. Steel, D. Gammon, D. S. Katzer, D. Park, C. Piermarocchi and L. J. Sham, Rabi oscillations of excitons in single quantum dots, *Phys. Rev. Lett.* **87** (2001) 133603.
41. I. N. Stranski and L. Krastanow, Stizungsberichte d. mathem.-naturw. Kl., Abt. IIb **146** (1938) 797.
42. K. Tachibana, T. Someya, S. Ishida and Y. Arakawa, Selective growth of InGaN quantum dot structures and their microphotoluminescence at room temperature, *Appl. Phys. Lett.* **76** (2000) 3212.
43. S. Tarucha, D. G. Austing, T. Honda, R. J. van der Hage and L. P. Houwenhoven, *Phys. Rev. Lett.* **77** (1996) 3613.
44. L. P. Kouwenhoven, T. H. Oosterkamp, M. W. S. Danoesastro, M. Eto, D. G. Austing, T. Honda and S. Tarucha, *Science* **278** (1997) 1788.
45. J. Vukovic, Photonic crystal structures for efficient localization of extraction of light, Ph.D. thesis, California Institute of Technology, Pasadena, CA, 2002.
46. D. O. S. Wei, Quantum computing with quantum dots, UROPS Paper (Module PC3288), Department of Physics, National University of Singapore (2003).
47. F. Widmann, J. Simon, N. T. Pelekanos, B. Daudin, G. Feuillet, J. L. Rouviere and G. Fishman, Giant piezoelectric effect in GaN self-assembled quantum dots, *Microelectronics J.* **30** (1999) 353–356.

48. http://britneyspears.ac/physics/crystals/wcrystals.htm
49. http://www.qubit.org
50. http://xxx.lanl.gov/archive/quant.ph
51. http://pages.ief.u-psud.fr/QDgroup/quantuminformation.html
52. http://www.nanotech.org/?path=Research/Optical/sQuantum/sDots
53. http://vortex.tn.tudelft.nl/grkouwen/kouwen.html
54. http://www.nd.edu/~qcahome